Master Thesis

Erasmus Mundus Master in Decentralized Smart Energy Systems,
with Thermal Energy Specialization

Development of a simulation tool for pebble heaters as part of energy savings and decarbonization for steel plants

REPORT

Author:	Delight Uchechukwu Ezeh
Director:	Jesus Castro Gonzalez (UPC)
Co-directors:	Akshay Bansal, Antoine Moussalem(ArcelorMittal)
Call:	July 2024

ETSEIB

Escola Tècnica Superior
d'Enginyeria Industrial de Barcelona

UPC

ETSEIB

Resum

(Abstract in Catalan)

La producció d'acer és un procés molt intensiu en energia i emissions, i amb el seu augment previst en el futur, a causa de la vitalitat de l'acer en el funcionament, el sosteniment i el desenvolupament de les economies modernes, hi ha una gran necessitat de solucions, vies i metodologies per augmentar la sostenibilitat dels processos d'elaboració d'acer en totes les facetes de producció, per assolir els objectius globals d'energia i clima. Els sistemes d'escalfament de llit de còdols/emmagatzematge d'energia tèrmica (TES) tenen un gran potencial per ser utilitzats com a regeneradors per recuperar la calor residual a totes les facetes de les plantes siderúrgiques. Així, aquesta tesi se centra en el desenvolupament d'una eina de simulació d'escalfadors de còdols mitjançant la modelització numèrica de la transferència de calor i la seva parafernàlia dins de sistemes TES de llit empaquetat, com a instrument preliminar per a provar casos d'ús i optimitzar les decisions de disseny per a la seva incorporació als processos de producció d'acer d'ArcelorMittal. , per permetre finalment l'estalvi energètic i la descarbonització.

El projecte es va dur a terme mitjançant l'execució d'una revisió exhaustiva de la literatura i una enquesta sobre les tècniques de modelització de la transferència de calor dels dispositius d'emmagatzematge de calor de llit empaquetat utilitzats en indústries pesades i, posteriorment, desenvolupant un model més robust com a millora de l'existent anteriorment a ArcelorMittal. El model finalment desenvolupat va ser un model 1D de dues equacions, calculat numèricament mitjançant el mètode de diferències finites amb un esquema d'integració temporal implícita. El model es va verificar i també es va validar mitjançant dades experimentals informades de fonts bibliogràfiques. Una anàlisi de sensibilitat en percentatge realitzada mitjançant el model va revelar la importància d'optimitzar la capacitat calorífica específica de les partícules sòlides, l'alçada de l'escalfador de còdols i el temps de càrrega, per maximitzar l'extracció d'energia de la font de calor residual. També es va demostrar que el diàmetre de les partícules sòlides afectava la conductivitat tèrmica efectiva del sistema TES (a causa de la seva proporcionalitat directa a la contribució radiativa de la conductivitat tèrmica), alhora que influïa en la caiguda de pressió a tot el sistema. Finalment, es van fer algunes propostes per millorar encara més el model dins de l'àmbit de la robustesa del model, i es van esmentar encertadament algunes activitats futures al voltant dels terminis de la tesi.

Resumen

(Abstract in Spanish)

La producción de acero es un proceso que consume mucha energía y emisiones, y con su aumento proyectado en el futuro, debido a la vitalidad del acero en la operación, el sustento y el desarrollo de las economías modernas, existe una enorme necesidad de soluciones, caminos y Metodologías para aumentar la sostenibilidad de los procesos de fabricación de acero en todas las facetas de la producción, para cumplir con los objetivos energéticos y climáticos globales. Los sistemas de calentadores de lecho de guijarros/almacenamiento de energía térmica (TES) poseen un gran potencial para usarse como regeneradores para recuperar el calor residual en todas las facetas de las plantas siderúrgicas. Así, esta tesis se centra en el desarrollo de una herramienta de simulación para calentadores de guijarros mediante el modelado numérico de la transferencia de calor y su parafernalia dentro de sistemas TES de lecho empacado, como instrumento preliminar para probar casos de uso y optimizar decisiones de diseño para su incorporación en los procesos de producción de acero de ArcelorMittal. , para, en última instancia, permitir el ahorro de energía y la descarbonización.

El proyecto se llevó a cabo mediante la ejecución de una revisión exhaustiva de la literatura y un estudio sobre técnicas de modelado de transferencia de calor de dispositivos de almacenamiento de calor de lecho empaquetado utilizados en industrias pesadas y, posteriormente, desarrollando un modelo más robusto como mejora del modelo previamente existente en ArcelorMittal. El modelo finalmente desarrollado fue un modelo 1D de dos ecuaciones, calculado numéricamente utilizando el método de diferencias finitas con un esquema de integración temporal implícito. El modelo fue verificado y también validado utilizando datos experimentales obtenidos de fuentes bibliográficas. Un análisis de sensibilidad porcentual ejecutado utilizando el modelo reveló la importancia de optimizar la capacidad calorífica específica de las partículas sólidas, la altura del calentador de guijarros y el tiempo de carga, para maximizar la extracción de energía de la fuente de calor residual. También se demostró que el diámetro de las partículas sólidas afecta la conductividad térmica efectiva del sistema TES (debido a su proporcionalidad directa con la contribución radiativa de la conductividad térmica), al tiempo que influye en la caída de presión en todo el sistema. Finalmente, se hicieron algunas propuestas para seguir mejorando el modelo dentro del alcance de la robustez del modelo, y se mencionaron acertadamente algunas actividades futuras relacionadas con los cronogramas de la tesis.

Abstract

Steel production is a very energy-and-emission-intensive process, and with its projected increase in the future, due to steel's vitality in the operation, sustenance, and development of modern economies, there is a huge need for solutions, pathways, and methodologies to increase the sustainability of steel making processes across all production facets, to meet global energy and climate goals. Pebble bed heaters/ Thermal Energy Storage (TES) systems possess great potential to be used as regenerators to recover waste heat across all facets of steel plants. Thus, this thesis focuses on the development of a simulation tool for pebble heaters via numerical modelling of heat transfer and its paraphernalia within packed bed TES systems, as a preliminary instrument for testing use cases and optimizing design decisions for their incorporation in ArcelorMittal's steel production processes, to ultimately enable energy savings and decarbonization.

The project was carried out by executing a thorough literature review and survey on heat transfer modelling techniques of packed-bed heat storage devices used in heavy industries and afterwards, developing a more robust model as an improvement to the previously existing one in ArcelorMittal. The finally developed model was a 1D, two-equation model, numerically computed using the finite difference method with an implicit time integration scheme. The model was verified and also validated using experimental data reported from literature sources. A percentage wise sensitivity analysis executed using the model revealed the importance of optimising the specific heat capacity of the solid particles, the height of the pebble heater and the charging time, to maximize energy extraction from the waste heat source. The diameter of the solid particles was also shown to impact the effective thermal conductivity of the TES system (due to its direct proportionality to the radiative contribution of the thermal conductivity), while also influencing the pressure drop across the system. Finally, some proposals were made for further improvement of the model within the model robustness scope, and a few future activities surrounding the thesis timelines were aptly mentioned.

ETSEIB

Acknowledgement

I wish to express my sincere, heart-felt gratitude to everyone and every organization who helped to make this thesis a success. In no particular order, I would like to thank the DENSYS consortium, whose aid and financial support is the foundational reason for my being involved in a quintessential master thesis project like this; from the President – Fabrice Lemoine, to the Vice President – Heathcliff Demaie, to the Project Manager - Samira Menouar and the UPC track co-ordinator – Quim Rigola, I say a very big “thank you!”.

I would also like to specially thank my thesis tutors at ArcelorMittal: Akshay Bansal and Antoine Moussalem, first for granting me the opportunity to do a thesis within their awe-inspiring purview, and also for their unflinching, unparalleled and practical support and guidance throughout the course of this work. I would also like to acknowledge the other members of the Energy and CO_2 team in ArcelorMittal – Gerald, Raphael and Elise, who provided feedback, insights and direction to me at one point or the other during the thesis.

This acknowledgement would not be complete without a special appreciation to my erudite academic supervisor from UPC – Jesus Castro Gonzalez, whose sturdy guidance, support and perspectives, aided the completion of this thesis work.

Finally, I would like to acknowledge my parents – Mr & Mrs Ezeh, my siblings, friends and well-wishers who supported me one way or another through the course of this thesis. I am genuinely grateful.

Content

List of symbols and Abbreviations

List of Abbreviations

TES	Thermal Energy Storage
PBTES	Pebble Bed Thermal Energy Storage
HTF	Heat Transfer Fluid
CSP	Concentrated Solar Plants
CFL	Courant–Friedrichs–Lewy
GS	Gauss-Seidel

List of Symbols

Symbols

D_P	Pebbles/Solid Particle Diameter
A_p	Pebbles/Solid Particle Surface Area
V_p	Pebbles/Solid Particle Volume
d_e	Pebbles/Solid Particle Effective diameter
d	Diameter (of other things)
H	Section Height
ε	Void factor (Porosity)
S_f	Shape Factor/Sphericity
a_{sv}	Solid particle surface area per unit bed volume
a_w	Wall Surface area per unit bed volume

S	Cross sectional area
ρ	Density
c_p	Specific heat capacity
λ	Thermal Conductivity
α	Thermal Diffusivity
u	Velocity
$\vec{v}$	Velocity vector
$\vec{\tau}$	Shear stress
g	Gravitational force
Q_v	Volumetric flow rate
μ	Dynamic viscosity
h	Convective heat transfer coefficient
h^*	Adjusted heat transfer coefficient
$\vec{q}^R$	Heat flux due to radiation
U_{loss}	Overall heat transfer coefficient for losses to the environment
T	Temperature
P	Pressure
R	Molar gas constant
ϕ	Contact Factor
B	Form Factor
ϵ	Emissivity
σ	Stefan-Boltzmann's constant
x_R	Effective radiation length

ETSEIB

f PBTES Tortuosity

Subscripts

s Solid

f Fluid

w Wall

ext External

ambient Surrounding environment

z Nomenclature of arbitrary node position

nz-1 Nomenclature of last node

Superscripts

n Previous time step

$n+1$ Present time step

o Adjusted Nomenclature for previous time step

Dimensionless numbers

Bi Biot's Number

Nu Nusselt Number

Re Reynolds Number

Pr Prandtl Number

Ra Rayleigh's Number

Gr Grashof's Number

List of figures

List of tables

ETSEIB

Preface

ArcelorMittal is a world leading steel company, with 126,756 employees in more than 60 countries. It has led the consolidation of the world steel industry, ranking today as the only truly global steelmaker with an industrial presence in 27 countries, while also leading in all major global markets, including automotive, construction, household appliances and packaging. As a global steel leader, ArcelorMittal's Global R&D spans the Globe with 14 sites dedicated to research (operating in process, products, application and steel solutions) within 9 countries, including the Maizières-lès-Metz R&D campus – where this thesis was carried out. ArcelorMittal is committed to reducing its carbon footprint as a responsible steel company and is executing this through various research focus across numerous frontiers. The work reported in this thesis falls within one of those frontiers that show the company's commitment towards solving the problems of decarbonization, circularity and energy sustainability within the steel and iron-making ecosystem.

1. Introduction

1.1. Background and Relevance of Study

Steel production is an energy-and-emission-intensive process, and its global industry is a very humongous one, churning out approximately 2 billion tonnes of steel per year, and accounting for about 8% of the global energy demand, while emitting a 7% share of the global CO_2 emissions that corresponds to 2.6 gigatonnes of carbon dioxide (Gt CO_2) [1]. Ranking as the highest emitter of CO_2 and second highest energy consumer amongst the heavy-duty industries, the steel industry is in the spotlight for rapid decarbonization and sustainability. However, unlike some other commodities whose use and production curtailment could be a major sustainability pathway, the production of steel is projected to increase in the future, as it is very vital to the operation, sustenance and development of modern economies and is even slated to be an integral ingredient for the energy transition by featuring in the production of wind turbines, dams, solar panels electric vehicles, etc. Thus, there is a huge demand for solutions, pathways, and methodologies to increase the sustainability of steel production across all production facets and meet global energy and climate goals – which require that emissions from the steel industry decrease by at least 50% by 2050 with further pursuit towards net zero emissions [1].

ArcelorMittal as a world leading steel company in all major global markets as well as R&D and technology, is heavily committed to decarbonization and sustainability of its steel making process, having set targets of reducing CO_2 emissions intensity by 25% and 35% in the global group and in Europe respectively by 2030, and attaining carbon neutrality in its global operations by 2050, alongside its aspirations of reducing energy consumption from the current 23 Giga Joules per tonne of steel produced (GJ/t) to a target value corresponding to Best Available Technologies (BAT) value of roughly 18GJ/t-steel [2]. Amidst its various strategies engaged to achieve these goals, is the energy performance improvement approach slated to increase the energy efficiency of its steel processes through heat recovery and repurposing. A major past example of the execution of this strategy within ArcelorMittal's ecosystem is the installation of checker-brick regenerative towers – which have been often coupled with blast furnaces to transfer heat in a regenerative way, from off gases exiting the furnace, to the hot blast air used in the blast process. However, outsourcing this heat recovery system to other processes in the steel making ecosystem proves to be very impractical due to factors like cost effectiveness, complex and multiple waste heat recovery and valorisation points, low-frequency-high-temperature-difficult-to-recover fumes, etc. Pebble heaters or pebble bed Thermal Energy Storage (TES) systems, nonetheless, have shown great potential to fill this regeneration expansion gap because of their potential flexibility and cost effectiveness and are thus being currently explored by ArcelorMittal as a novel tool to increase energy efficiency within its processes.

Incorporation of these pebble bed TES (PBTES) into ArcelorMittal's processes on an industrial scale requires a thorough design and simulation procedure within the frameworks of the intricacies and nuances of the company's processes. This includes, but is not limited to experiments, numerical and simulation analysis, pilot tests, etc. of the pebble bed heaters for different configurations and cases. This project/thesis is slated to contribute towards these aspects by focusing on the development of a simulation tool for the pebble heater via numerical modelling of heat transfer and its paraphernalia, within the packed bed storage, as a preliminary instrument for testing use cases and optimizing design decisions for the incorporation of pebble bed heaters in ArcelorMittal's steel production processes, to ultimately enable energy savings and decarbonization on a large scale.

1.2. Scope and Objectives

To carry out this project/thesis, the following aims and objectives are established.

i. Thorough literature review and survey on numerical heat transfer modelling of conventional and novel packed bed TES systems applied to heavy duty industries.
ii. Improvement and development of algorithm, numerical models, and corresponding codes for existing and novel packed bed TES systems.
iii. Analysis of obtained results and comparison with experimental results, where available.
iv. Application of model for testing use cases and optimizing design decisions.

2. Literature Review

Pebble heaters are a type of packed-bed regenerative heat exchanger, and have been employed in various settings to improve energy efficiency or to simply just store heat. For instance, they are often used as storage systems in Concentrated Solar Plants [3], and Solar Gas Turbine cycles [4], and are also largely used for waste heat recovery in heavy duty industries within various configurations [5][6]. Pebble heaters are of different types and could be classified based on the way they store heat, the direction of flow of the energy vector, the type of energy vector used for the heat transfer, etc. Based on the way heat is stored, pebble heaters could be classified into: sensible heat PBTES, latent heat PBTES and chemical heat PBTES [7], based on the flow direction of the energy vector, they could be mainly classified into axial and radial PBTES [8], and based on the energy vector used for heat transfer, they could be classified into gas-solid PBTES and liquid-solid PBTES.

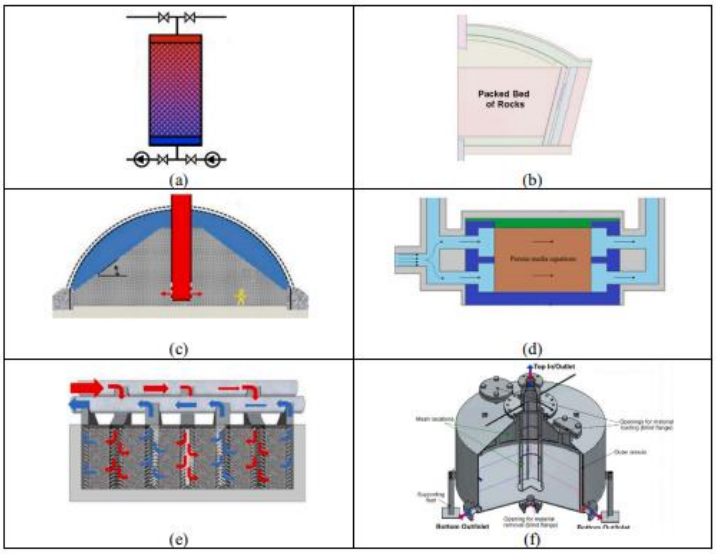

Figure 2.1: Main Packed bed TES designs (a) traditional cylindrical PBTES with axial HTF flow (b) buried truncated conical TES with axial HTF flow (c) self-insulated unconstrained PBTES (d) horizontal flow PBTES (e) modular layered PBTES with horizontal flow (f) radial-flow PBTES [8]

The type of PBTES determines the approach, scope and robustness of the modelling techniques that could be used to model the pebble heater, and as such, in some cases, models cannot be used interchangeably. This underscores the importance of a careful understanding of each modelling technique, with a special emphasis on the assumptions considered, which is most often a function of the type of PBTES being modelled.

2.1. Modelling Techniques – Broad Classification

The fundamental heat transfer principles for all the packed bed systems take root from the heat transfer principles in a porous media – which has been explored extensively in the past. From a general point of view, in a porous media like the PBTES, the three different heat transfer phenomena: radiation, convection and conduction occur as shown in Figure 2.2, however, since 1929 – when Schumann developed an analytical model for analysing the heat transfer of the system of a liquid flowing through a porous prism [9], till now, various numerical models have been proposed and utilized by several researchers to simplify the simulation of the heat transfer in a packed bed TES, and these models often choose and make appropriate assumptions and simplifications to the actual heat transfer phenomenon in the PBTES, thereby simplifying the general energy equation format shown in equation 2.1into different forms.

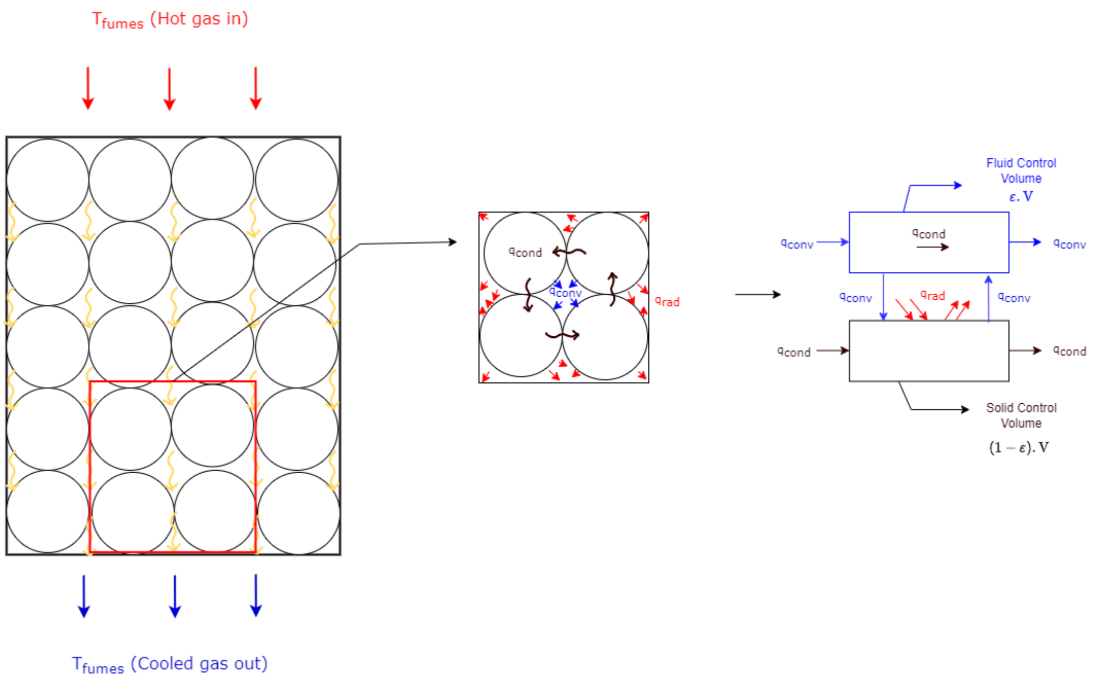

Figure 2.2: Evolution of the description of heat transfer in a PBTES

$$\begin{aligned} &Energy\ Accumlation\ term + Convective\ term = Conduction\ (Diffusive)\ term \\ &\quad + Source\ terms\ + Other\ terms \end{aligned} \qquad 2.1$$

These models could be largely classified into four different kinds namely: the Schuman's model, the continuous solid model, the single phase/one-equation model and the thermal gradient model [10]. Most research involving numerical modelling of packed bed thermal energy storage often utilized one or more of these modelling styles, usually in their 1-D format and with additional modifications and nuances in some cases. Asides the single equation model, all aforementioned modelling classifications utilize separate energy equations for the fluid and the porous media or solid, which tends to separately analyse the materials of the packed bed TES system while accounting for their fusion through some heat transfer and flow terms alongside the specification of the porosity. Moreover, with the exception of the thermal gradient model, the models also generally assume very small solid particle sizes, such that each particle could be considered to have a uniform temperature across the whole volume.

The Schumann's model, assumes that heat transfer by conduction within the fluid itself of the solid is negligible compared to heat transfer from the fluid to the solid and vice versa, thus neglecting the conduction terms for both the fluid and the solid thermal equations. It also neglects changes in volume of fluid and solid due to change in temperature while also positing that the heat transfer across the fluid and solid is proportional to the average difference in fluid and solid temperature at any given point [9] [10]. The continuous solid model captures the conduction heat transfer in both the fluid and the solid equations as well as the losses between the packed bed TES system and the ambient.

The single phase/one-equation model assumes that the thermal conductivity and thermal capacity of the solid is very high compared to that of the working fluid, and as such the instantaneous temperatures of both the solid and the fluid phases are equal, thus modelling the two material phases as one, while using equivalent material and thermophysical properties. The thermal gradient model considers the thermal gradients inside the solid particles, and as such does not posit interparticle heat transfer, thus, the temperature gradients at surfaces only occur due to heat transfer between the fluid and the external surface of the solid particles, despite using the two-equation system. In other words, the solid equation for this modelling technique only possesses the accumulation and conduction term.

2.2. Nuances to broadly classified modelling techniques

Modifications were made to the Schuman's model by Walter et al while performing a computational simulation of an experimentally tested 100 kWh_{th} radial packed bed for thermal energy storage (TES) using a 1D radial MATLAB model [11]. The conduction term alongside a term modelling the heat loss to the surrounding environment were added to accurately simulate the long-duration storage. Also, the mass flow rate was specified at every instant in time, and was assumed to be spatially constant, while the superficial gas velocity and the local gas velocity (assumed constant in the Schumann's model) varied with both temperature and with radius in the radial and spherical configurations. Trevisan et al also made similar modifications to the Schumann's model in an axial TES configuration during a study on the analysis and optimization of a packed bed thermal energy storage and the influence of quasi-dynamic boundary conditions on the storage thermodynamic performance, detailing the derivation of the overall heat transfer coefficient for the heat loss term [3].

The continuous solid model was often used without modification to the equation as implemented by the likes of Ortega et al who analysed the operation of a packed bed TES system comprising of EAF steel slag using CFD to obtain flow parameters [6]. Anderson et al also used the same model to predict the fluid and solid temperatures in a packed bed thermal energy storage vessel that used compressed gas as the heat transfer fluid [12]. Marongiu et al took the model to the 2D domain during the development of a two-dimensional model of an existing high temperature thermal energy storage rock bed unit of 450 kWh_{th} thermal capacity [13], and Trevisan et al used a radial 1-D version during the thermal and hydrodynamic modelling of a proposed multi-layered packed bed TES with two and three coaxial layers, while detailing the formulation for computing the effective thermal conductivities of both the fluid and solid to capture the radiation effects [8].

Anderson et al in another research set out to show and validate the usability and simplicity of the single phase/one equation model by modelling a Concentrated Solar Power plant's packed bed energy storage, configured to use alpha alumina balls as solid material and air as heat transfer fluid [14]. The flow properties of the model were characterized using the Navier-Stokes equation, which was solved using CFD, and more importantly, the importance of variable temperature dependent thermophysical properties in models was established through a detailed additional study of air and alumina at variable temperature levels getting as high as 700ºC in some scenarios. It was observed by the authors that the difference between using an average temperature for the calculation and using the temperature-dependent properties were more substantial at higher temperatures, with the errors being slated to compound through multiple cycles.

Zou et al developed an explicit model for a porous-medium configuration which predicts both macroscopic (pebble bed) and microscopic (pebble) temperature distributions in both steady-state and transient scenarios [15]. The model employed a one-dimensional transient heat conduction equation in spherical coordinates for pebbles and was ultimately shown to accurately capture the stored thermal energy in a pebble bed. Despite the advent of the expansion of this methodology, the earlier developed formulation proposed by Xu et al [16], for an effective fluid and solid convective heat transfer co-efficient for large Biot number configurations, as a method of ascertaining a wide range of operation beyond the assumption of small particle size and uniform temperature distribution within each solid particle, is still being used to expand the validity of models due to its computational simplicity [8].

2.3. Nusselt number computation

The Nusselt number correlations used to compute the convective heat transfer coefficients in the energy equations also varied based on applications and flow characterizations specific to the scenario of the cases being modelled. Ortega et al for instance used Nusselt number correlations from Pfeffer et al [17] for low Reynold number cases (Re_p < 15) and correlations from Alamzi and Vafai [18] for higher Reynold numbers (Re_p ≥ 15) [6]. Walter et al analysed six different Reynold number formulations [11] which showed a fair agreement over the Reynolds number range: 0 to 1000. However, the Gunn model was chosen because it included the porosity as a parameter and was the only model, according to Walter et al, found in the literature that appears to be valid within the range 0 < Re < 20. Trevisan et al used a direct correlation for the convective heat transfer coefficient proposed by Coutier and Faber [19] because it was obtained through different experimental setups, with the consideration of some minor phenomena, thereby helping to avoid further modelling steps [3]. Nonetheless, in a later work [8], Trevisan et al used the Nusselt number formulated by Wakao et al [20], which is valid for a Reynold number range of 15 < Re < 8500, with Marongui et al also doing same for the 2D rock bed numerical model.

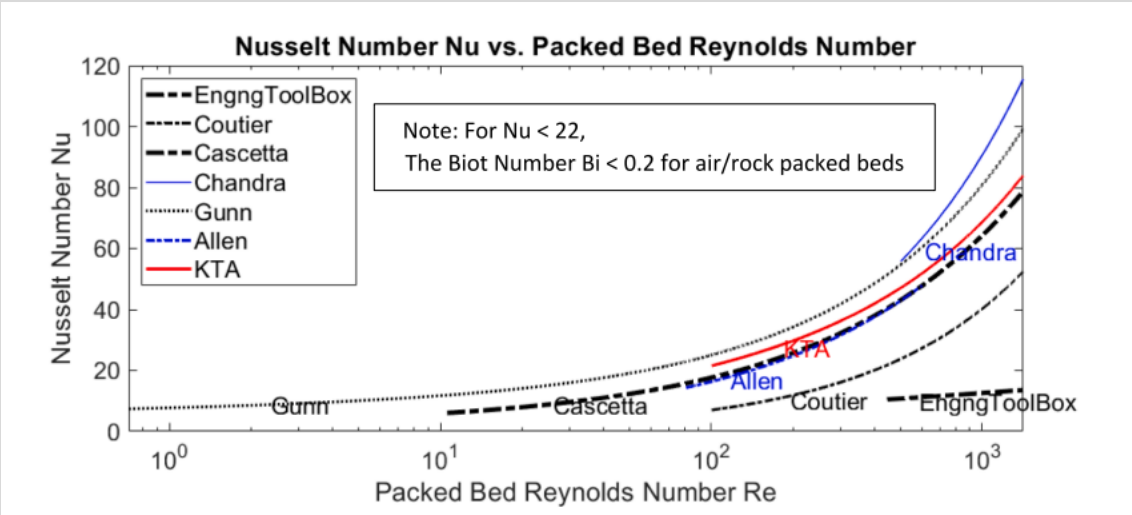

Figure 2.3: Nusselt number vs Reynolds number for air HTF in a packed bed according to various researchers as reported by Walter et al [11]

2.4. Effective thermal conductivity and radiation modelling

The thermal conductivity used in the diffusive/conductive term of the modelling equations is also of utmost importance and has been widely studied, with various best practice formulations being proposed depending on the modelling technique. For the one-equation, model, the focus is usually on computing a single value for effective thermal conductivity of the whole porous media, considering the thermal conductivities of the solid, the fluid and in some high temperature scenarios, the radiative heat transfer. Nield in 1991, [21] developed a simple correlation for assessing the effective thermal conductivity of packed beds based on a void fraction-weighted geometric average of fluid and solid conductivities, however, the most popular formulation being used is that of Zehner and Schlünder [22] who established a reference model (ZS model) for calculating the effective conductivity of a unit cell comprising fluid and solid phases, by using results from mass transfer experiments to correlate the influence of void fraction. Radiative contributions to the effective thermal conductivity were computed by the likes of Sih and Barlow [23] and Breitbach and Barthels [24] who all referred to the unit cell approach captured by the ZS model. Models who employed any two-equation approach often went beyond obtaining the effective thermal conductivity of the media, to actually divide or share it between the fluid and solid phases [3][8], referring to the methodology highlighted by Cheng and Hsu [25], who devised a method to do so, by using the tortuosity of the bed.

2.5. Pressure drop modelling.

Pressure drops within the packed bed have been largely modelled using the Ergun's equation [26], often implemented for both radial and axial configurations [11][6][8]. Nevertheless, Walter et al [11] also considered the Kozeny-Carman equation – which assumes laminar flow in its configuration, and Marongui et al used the continuity equation and the Brinkman's equation for porous media flow, to cater for the mass and momentum balances in the model [13]. Solving the Navier-Stokes equation using CFD was also another route taken to cater for the pressure changes in the packed bed models [14].

2.6. Model Validation techniques

Model validation was often executed by ascertaining reasonable agreement between the model results and the experimental data of the cases being numerically modelled [11][12][13][14], or with analytical solutions [15][16]. However, in cases where such were not available, the validation was done using authenticated experimental data outsourced from other research works. For instance, Ortega et al demonstrated accuracy of their model by comparing and validating numerical results of spatial temperature distribution over time, with the experimental results published by Klein et al [4]. Trevisan et al opted for the same modelling methodology by comparing the model results with experimental results from Hanchen et al [27] and Meier et al [28]. However, apart from Ortega et al who explicitly expressed the criteria for validation on the premise that the mean absolute error between the numerical model and the experimental model was 3% [6], majority of the research work simply displayed the comparison plot, commented on the disparities, and stated that the results were in good agreement. Despite the fact that such claims were palpable on the premise of the similarities of results, there have been no established and concise statements on any validation criteria or allowable error margin that should exist between the validation data and computed model results.

3. Methodology

3.1. General Overview

Approaching the execution of the objectives of the thesis required an acute methodological process to obtain the best results as optimally as possible. The literature review was carried out with a special focus on the application of PBTES in heavy duty industrial applications like CSP and industrial waste heat management. The objective of the literature review was to explore various modelling techniques employed vis a vis the assumptions and approximations employed, in order to have a robust perspective to make candid and optimal model improvement suggestions to ArcelorMittal's preliminary PBTES model. After the literature review, a thorough top-down analysis of the existing PBTES model was performed, to understand the scope, sophistication and limitations of the model, from both a physical and computational point of view. Next, model improvement suggestions were proposed and prioritized based on ArcelorMittal's needs, and the needed adjustments were executed step by step based on the priority list. After the adjustments, were made, a thorough search was executed to find suitable externally performed experimental data to use for the model's validation, after which the model was validated. The existing model was created in python, and as such, all the other improvements were made in the same programming language, with the model for the fluid thermophysical properties being sourced from Cantera [29] – a python based open-source suite of tools for problems involving chemical kinetics, thermodynamics, and transport processes. The following sections describe the methodology and formulation for the aforementioned processes in greater detail.

3.2. Analysis of previously existing model

This section describes the methodology and formulation of ArcelorMittal's existing model, and the importance of its capture lies in the fact that it is the model upon which further improvements and additions are to be made, and a proper understanding of its formulation, shapes the foundation for any enhancement. The formulation for any heat transfer modelling in a porous medium takes root in the general continuity, momentum, energy and specie transfer equations which are captured in equations 3.1, 3.2, 3.3, 3.4 below respectively [30] .

$$\frac{\partial \rho}{\partial t} + \nabla \cdot (\rho \vec{v}) = 0 \tag{3.1}$$

$$\frac{\partial (\rho \vec{v})}{\partial t} + \nabla \cdot (\rho \vec{v}\vec{v}) = \nabla \cdot (\mu \nabla \vec{v}) + \nabla \cdot (\vec{\tau} - \mu \nabla \vec{v}) - \nabla p + \rho \vec{g} \tag{3.2}$$

$$\frac{\partial (\rho T)}{\partial t} + \nabla \cdot (\rho \vec{v} T) = \nabla \cdot \left(\frac{\lambda}{c_p} \nabla T\right) + \left\{\frac{-\nabla \cdot \vec{q}^R - p \nabla \cdot \vec{v} + \vec{\tau} : \nabla \vec{v}}{c_p}\right\} \tag{3.3}$$

$$\frac{\partial (\rho Y_k)}{\partial t} + \nabla \cdot (\rho \vec{v} Y_k) = \nabla \cdot (\rho D_{km} \nabla Y_k) + \dot{\omega}_k \tag{3.4}$$

The terms highlighted in red represent the unsteady or accumulation term, the terms in blue are the convective terms, the terms in green are the diffusive terms and the terms in black consist of a block of other terms like radiation and source terms in the energy equation, body and viscous forces in the momentum equation, etc. A couple of assumptions were imposed on these general equations to produce ArcelorMittal's previously existing PBTES model and these assumptions are as follows:

i. Application of a 1D continuous-solid, two-equation modelling technique in the axial configuration.
ii. Species transfer is negligible and fluid flow is incompressible ($\mathrm{Ma} < 0.2$)
iii. Pressure losses are negligible; thus, flow properties are pressure independent
iv. Radiation heat transfer is negligible.
v. Heat losses from the PBTES to the environment are negligible.
vi. $Bi < 0.1$ for the solids, and as such, thermal gradients within solid particles are negligible.
vii. Thermophysical properties of the solids are temperature independent.

Upon application of these assumptions to the general equations, the pre-existing model equations were formulated viz:

For the energy equation:

$$(1-\varepsilon)(\rho c_p)_s \left(\frac{\partial T_s}{\partial t}\right) = (1-\varepsilon)\frac{\partial}{\partial z}\left(\lambda_s \frac{\partial T_s}{\partial z}\right) + h a_{sv}(T_f - T_s) \tag{3.5}$$

$$\varepsilon(\rho c_p)_f \left(\frac{\partial T_f}{\partial t}\right) + (\rho c_p)_f \left(u_f \frac{\partial T_f}{\partial z}\right) = \varepsilon \frac{\partial}{\partial z}\left(\lambda_f \frac{\partial T_f}{\partial z}\right) + h a_{sv}(T_s - T_f) \tag{3.6}$$

Equation 3.5 and equation 3.6 represent the energy equations for the solid and the fluid respectively and it could be seen that they are both linked by the last term in each equation, which represents the convective heat transfer exchange between the fluid and the solid. It is important to note that the thermophysical properties of the fluid were not assumed to be temperature independent like those of the solid.

The equations were numerically resolved using the finite difference method, whose solution begins with a numerical discretization of the partial differential equations – which was executed using the second order Taylor's series expansion for the diffusive terms, and an upwind difference scheme for the convective term. The time derivative was afterwards resolved using the explicit time integration (forward Euler) scheme where the next time step's variables are calculated with variables from the previous time step. Executing the numerical resolution described above to both equations would give the following:

For the Pebbles (Solid)

Re-writing equation 3.5 in the normal differential form and making the time dependent term the subject of the formula will give:

$$\frac{dT_s}{dt} = \frac{1}{\left(\rho c_p\right)_s}\frac{d}{dz}\left(\lambda_s \frac{d}{dz}\right) + \frac{h a_{sv}}{(1-\varepsilon)\left(\rho c_p\right)_s}\left(T_f - T_s\right) \qquad 3.7$$

Assuming constant values for material properties will give:

$$\frac{dT_s}{dt} = \frac{\bar{\lambda}_s}{\bar{\rho}_s \bar{c}_{p_s}}\frac{dT_s{}^2}{dz^2} + \frac{h a_{sv}}{(1-\varepsilon)\bar{\rho}_s \bar{c}_{p_s}}\left(T_f - T_s\right) \qquad 3.8$$

Applying second order Taylor's series expansion to the second order differential conduction term would give:

$$\frac{dT_{s,z}}{dt} = \bar{\alpha}_s\left(T_{s,z+1} - 2T_{s,z} + T_{s,z-1}\right) + \beta_{s,z}\left(T_{f,z} - T_{s,z}\right) \qquad 3.9$$

Where:

$\bar{\alpha}_s \approx \frac{\bar{\lambda}_s}{\bar{\rho}_s \bar{c}_{p_s}}$

$a_{sv} = \frac{6(1-\varepsilon)}{d_e \cdot S_f}$

$d_e = D_p \cdot S_f$

$\beta_s = \frac{h_z a_{sv}}{(1-\varepsilon)\bar{\rho}_s \bar{c}_{p_s}}$

$S_f = \frac{\pi^{\frac{1}{3}}(6V_p)^{\frac{2}{3}}}{A_p}$

z = Position nomenclature for discretization of the solid domain

Applying the explicit time differential scheme to equation 3.9 would give the final discretization equation for the solid viz:

$$\frac{{T_{s,z}}^{n+1} - {T_{s,z}}^{n}}{\Delta t} = \frac{{\bar{\alpha}_s}^{n}\left({T_{s,z+1}}^{n} - 2{T_{s,z}}^{n} + {T_{s,z-1}}^{n}\right)}{\Delta z^2} + {\beta_{s,z}}^{n}\left({T_{f,z}}^{n} - {T_{s,z}}^{n}\right) \tag{3.10}$$

For the Fluid (Air or flue gases)

Re-writing equation 3.6 in the normal differential form and making the time dependent term the subject of the formula will give:

$$\frac{dT_f}{dt} = -\frac{1}{\varepsilon}\left(u_f\frac{dT_f}{dz}\right) + \frac{1}{\left(\rho c_p\right)_f}\frac{d}{dz}\left(\lambda_f\frac{dT_f}{dz}\right) + \frac{ha_{sv}}{\varepsilon\left(\rho c_p\right)_f}\left(T_s - T_f\right) \tag{3.11}$$

Applying second order Taylor's series expansion to equation 3.11 and using the upwind scheme for the convective scheme will give:

$$\frac{dT_f}{dt} = -\frac{u_f}{\varepsilon\Delta z}\left(T_{f,z} - T_{f,z-1}\right) + \frac{\alpha_{f,z}\left(T_{f,z+1} - 2T_{f,z} + T_{f,z-1}\right)}{\Delta z^2} + \beta_{f,z}\left(T_{s,z} - T_{f,z}\right) \tag{3.12}$$

Where:

$$\beta_f = \frac{ha_{\mathrm{sv}}}{\varepsilon\left(\rho c_{\mathrm{p}}\right)_f}$$

$$\alpha_f = \frac{\lambda_f}{\rho_f {c_p}_f}$$

$z =$ Position nomenclature for discretization of the liquid domain

The formulation for the velocity 'u_{f}' incorporates the continuity equation shown viz:

$$\dot{m}_1 = \dot{m}_2$$

$$\rho_1 S_1 u_1 = \rho_2 S_2 u_2$$

$$\frac{P_1}{R_1 T_1} S_1 u_1 = \frac{P_2}{R_2 T_2} S_2 u_2$$

Since the same material specie is being maintained, $R_1 = R_2$, thus,

$$u_2 = S_1 u_1 \frac{T_2}{T_1}\frac{P_1}{P_2} = \frac{Q_{v,1}}{S_1}\left(\frac{T_2}{T_1}\right)\left(\frac{P_1}{P_2}\right)$$

$Q_{v,1}$ is the volume flow rate, and at the entry point of the PBTES, it would be an input value normally measured, in Normal cubic meters per unit time (i.e corresponding value of pressure and temperature are in STP conditions - $0^oC\ , 1atm$), If the cross-sectional area in the flow direction remains the same, then the other fluid velocities along the flow path of the PBTES could be written in terms of the input fluid flow rate thus:

$$u_{\mathrm{f}} = \frac{Q_{v,N}}{S_{passage}}\left(\frac{T_f}{273.15}\right)\left(\frac{1}{P_f}\right) \tag{3.13}$$

Applying the explicit time differential scheme to equation 3.12 would give the final discretization equation for the fluid viz:

$$\frac{{T_{f,z}}^{n+1} - {T_{f,z}}^{n}}{\Delta t} = \frac{u_f}{\varepsilon \Delta z}\left({T_{f,z-1}}^{n} - {T_{f,z}}^{n}\right) + \frac{{\alpha_{f,z}}^{n}\left({T_{f,z+1}}^{n} - 2{T_{f,z}}^{n} + {T_{f,z-1}}^{n}\right)}{\Delta z^2} + {\beta_{f,z}}^{n}\left({T_{s,z}}^{n} - {T_{f,z}}^{n}\right) \tag{3.14}$$

The convective heat transfer coefficient in both the solid and fluid formulations is given by:

$$h = \frac{\lambda_f Nu}{d_e}$$

Where:

$$Nu = 2 + 1.1Re^{0.6} \cdot Pr^{\frac{1}{3}}$$

$$Re = \frac{\rho_f d_e u_f}{\mu_f}$$

$$\mathrm{Pr} = \frac{\mu_f c_{p,f}}{\lambda_f}$$

The Nusselt number formulation employed, as shown above was that purported by Wakao et al [20], due its validity for a porous medium like the PBTES over a wide range of Reynolds number.

Boundary Conditions

There are different configurations of flow through a PBTES as labelled by ArcelorMittal and those configurations determine the assignment of the boundary conditions. The first is the co-current configuration – which indicates a configuration where both charging the PBTES with a hot HTF (fumes) and discharging the PBTES with a cool HTF (blast air) is done from the top of the PBTES, and the second is the counter current configuration – where charging the pebble heater with the hot HTF is done from the top and discharging with a cold HTF is done from the bottom of the TES. The previously existing model was formulated for only the charging configuration as shown in Figure 3.1, and as such, the governing equations for the boundary conditions are as follows:

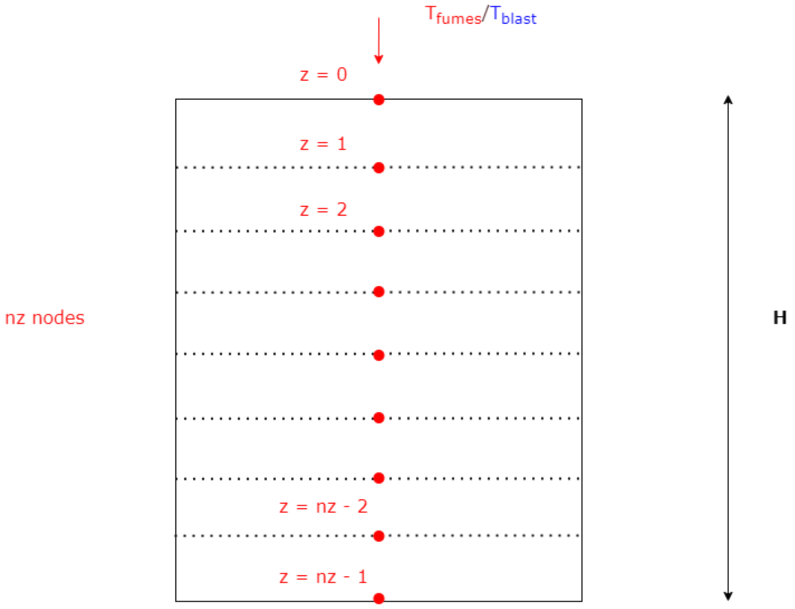

Figure 3.1: Discretization of PBTES in co-current configuration

Charging (with hot HTF/fumes)

For Node z = 0

$$\frac{T_{s,0}{}^{n+1} - T_{s,0}{}^{n}}{\Delta t} = \frac{\bar{\alpha}_s{}^{n}\left(T_{s,1}{}^{n} - T_{s,0}{}^{n}\right)}{\Delta z^2} + \beta_{s,0}{}^{n}\left(T_{f,0}{}^{n} - T_{s,0}{}^{n}\right) \tag{3.15}$$

$$\frac{T_{f,0}{}^{n+1} - T_{f,0}{}^{n}}{\Delta t} = \frac{u_{f,0}{}^{n}}{\varepsilon \Delta z}\left(T_{fumes,in}{}^{n} - T_{f,0}{}^{n}\right) + \frac{\alpha_{f,0}\left(T_{f,1}{}^{n} - 2T_{f,0}{}^{n} + T_{fumes,in}{}^{n}\right)}{\Delta z^2} + \beta_{f,0}{}^{n}\left(T_{s,0}{}^{n} - T_{f,0}{}^{n}\right) \tag{3.16}$$

For Node z = nz – 1

$$\frac{T_{s,nz-1}{}^{n+1} - T_{s,nz-1}{}^{n}}{\Delta t} = \frac{\bar{\alpha}_s\left(T_{s,nz-2}{}^{n} - T_{s,nz-1}{}^{n}\right)}{\Delta z^2} + \beta_{s,nz-1}{}^{n}\left(T_{f,nz-1}{}^{n} - T_{s,nz-1}{}^{n}\right) \tag{3.17}$$

$$\frac{T_{f,nz-1}{}^{n+1} - T_{f,nz-1}{}^{n}}{\Delta t} = \frac{u_{f,nz-1}{}^{n}}{\varepsilon \Delta z}\left(T_{f,nz-2}{}^{n} - T_{f,nz-1}{}^{n}\right) + \frac{\alpha_{f,nz-1}{}^{n}\left(T_{f,nz-2}{}^{n} - T_{f,nz-1}{}^{n}\right)}{\Delta z^2} + \beta_{f,nz-1}{}^{n}\left(T_{s,nz-1}{}^{n} - T_{f,nz-1}{}^{n}\right) \quad 3.18$$

Initial conditions

$T_{f,z}{}^{t=0} = T_{f,initial} \ \forall z = 0 \ to \ nz - 1$

$T_{s,z}{}^{t=0} = T_{s,initial} \ \forall z = 0 \ to \ nz - 1$

Discharging (with cold HTF/blast)

The formulations for the boundary conditions during the discharging phase in the co-current configuration is similar to the boundary conditions for the charging phase since in both cases, the HTF comes in from the top. However, the only adjustment is that $T_{fumes,in}$ becomes $T_{blast,in}$.

The discretization equations highlighted above (equations 3.10, 3.14, 3.15 - 3.18) were thus solved by making the Temperature of the present step the subject of the formula and ensuring to constrain both the time and space discretization within the limits of the CFL conditions.

3.3. Model Improvements

Having established the formulation of the previous or old model, certain improvements were subsequently proposed (with an order of priority) to make the existing model more realistic and computationally efficient, using perspectives obtained from the literature review. These improvement propositions are listed as follows in order of priority:

i. Conversion from explicit to the implicit time integration scheme. (P1)
ii. Introduction of effective thermal conductivity that considers both the porosity and some radiation heat transfer phenomenon.(P2)
iii. Inclusion of temperature dependent thermophysical properties for the PBTES solid. (P3)
iv. Capturing pressure drops and pressure dependency in flow properties like velocity through continuity and momentum equations.(P3)
v. Modified Convective heat transfer co-efficient to deal with higher Biot numbers (i.e Larger Pebbles/solid particles). (P4)
vi. Consideration of heat losses from the tank wall to the environment, etc. (P4)

All the proposed improvements were added to the existing model, while maintaining all other numerical resolution schemes (in the exception of the time integration scheme), and the justification and formulation for their incorporation are captured in the succeeding sub sections.

3.3.1. From explicit to implicit

There are several time integration schemes used to numerically approximate time differential calculations and they include the explicit (forward Euler) method, implicit (backward Euler) method, Crank Nicolson method, etc. The previously existing pebble bed model used the explicit time integration scheme which is a first order scheme where computation of the present time step or next time step's unknowns is made with properties and variables of the previous time step. This method offers an advantage of simplicity in computational solution; however, its use poses a limitation in computational time, efficiency, and resources due to CFL stability conditions that compulsorily constrain the time step used, to a fraction of the spatial mesh size – which is often made small for improved accuracy. Consequently, very small spatial mesh sizes lead to smaller time steps and a much longer computational time, which is quite impractical for pebble heat modelling where simulations are often made for test cases spanning hours and days. Thus, a switch to the implicit method was imminent. The implicit method is also a first order scheme (as shown in

Figure 3.2); however, calculation of the next time step's unknowns is executed with properties and variables of the present time step in consideration, thus, there are more unknowns to be computed. Despite the computational complexities in this scheme – which often leads to the use of matrices, solvers, etc., it does not have any stability condition related to the mesh size, hence, more reasonable time steps could be selected preferentially without limitations, leading to potentially faster computational durations that are compatible with the simulation of pebble bed heaters. It should be noted that the use of the implicit scheme does not necessarily imply a higher order accuracy of results because like the explicit scheme, it is also a first order time approximation scheme (see Figure 3.2). Improvement to a higher order accuracy would involve the use of schemes like the Crank Nicolson scheme – a second order scheme, as well as other higher order time integration schemes available.

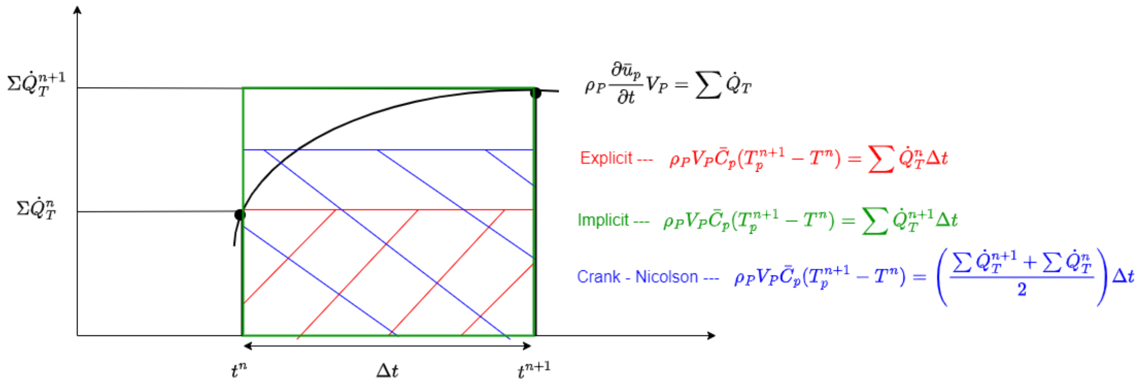

Figure 3.2: Pictorial overview of some time integration schemes.

Applying the implicit time integration scheme to the solid and fluid pebble equations in equations 3.7 and 3.12 respectively would give:

$$\frac{T_{s,z}{}^{n+1} - T_{s,z}{}^{n}}{\Delta t} = \frac{\bar{\alpha}_s{}^{n+1}\left(T_{s,z+1}{}^{n+1} - 2T_{s,z}{}^{n+1} + T_{s,z-1}{}^{n+1}\right)}{\Delta z^2} + \beta_{s,z}{}^{n+1}\left(T_{f,z}{}^{n+1} - T_{s,z}{}^{n+1}\right) \qquad 3.19$$

$$\frac{T_{f,k}{}^{n+1} - T_{f,k}{}^{n}}{\Delta t} = \frac{u_f{}^{n+1}}{\varepsilon \Delta z}\left(T_{f,k-1}{}^{n+1} - T_{f,k}{}^{n+1}\right) + \frac{\alpha_{f,k}{}^{n+1}\left(T_{f,k+1}{}^{n+1} - 2T_{f,k}{}^{n+1} + T_{f,k-1}{}^{n+1}\right)}{\Delta z^2} + \beta_{f,k}{}^{n+1}\left(T_{s,k}{}^{n+1} - T_{f,k}{}^{n+1}\right) \qquad 3.20$$

For the sake of simplicity, the superscript 'n', corresponding to the previous time step was substituted by 'o' and the super index '$n+1$' is simply dropped viz:

$$\frac{T_{s,z} - T_{s,z}{}^{o}}{\Delta t} = \frac{\bar{\alpha}_s\left(T_{s,z+1} - 2T_{s,z} + T_{s,z-1}\right)}{\Delta z^2} + \beta_{s,z}\left(T_{f,z} - T_{s,z}\right) \qquad 3.21$$

$$\frac{T_{f,z} - T_{f,z}{}^{o}}{\Delta t} = \frac{u_f}{\varepsilon \Delta z}\left(T_{f,z-1} - T_{f,z}\right) + \frac{\alpha_{f,z}\left(T_{f,z+1} - 2T_{f,z} + T_{f,z-1}\right)}{\Delta z^2} + \beta_{f,z}\left(T_{s,z} - T_{f,z}\right) \qquad 3.22$$

3.3.2. Effective thermal conductivity.

The effective thermal conductivity of a porous medium involves the calculation of the thermal conductivity of the matrix system as a function of both the packed solids and the fluid interstices comprising the porosity of the system. According to Esence et al [31], in a two-equation system for the heat transfer modelling of a porous medium, where the diffusive terms (which contains the thermal conductivity) are captured in both equations, the effective thermal conductivity of the whole system must be shared between the solid and the fluid, to obtain a solid effective thermal conductivity and fluid effective thermal conductivity. This same method was also utilized by Trevisan et al for the formulation of their model [3]. However, the previous PBTES model described in section 3.2 neither captured the concept of effective thermal conductivity, nor consider the effective thermal conductivity contribution of the solid and fluid. Thus, the improvement to the model had to capture this computational adjustment to make the model more realistic.

The first step of including this phenomenon involved the computation of the effective thermal conductivity for the porous media as a whole, factoring into account, the radiation heat transfer. This formulation was captured by Sih and Barlow [32], who modified the Zehner-Schlunder's equation [22] and it is given by:

$$\frac{\lambda_{eff}}{\lambda_f} = \left(1-\sqrt{1-\varepsilon}\right)\left(1+\frac{\varepsilon\lambda_R}{\lambda_f}\right) \tag{3.23}$$

$$+\sqrt{1-\varepsilon}\left\{(1-\phi)\left[\frac{2}{1-\frac{B\lambda_f}{\lambda_s}}\left(\frac{B}{\left(1-\frac{B\lambda_f}{\lambda_s}\right)^2}\left(1-\frac{\lambda_f}{\lambda_s}\right)ln\frac{\lambda_s}{B\lambda_f}-\frac{B+1}{2}-\frac{B-1}{1-\frac{B\lambda_f}{\lambda_s}}\right)+\frac{\lambda_R}{\lambda_f}\right]+\phi\frac{\lambda_{contact}}{\lambda_f}\right\}$$

Where:

λ_{eff} = Effective thermal conductivity corrected to include radiation effects (W/mK).

λ_f = Thermal conductivity of continuous gas phase (W/mK)

λ_s = Thermal conductivity of the skeletal solid (W/mK)

ε = Porosity of packed bed (void fraction)

B = form factor and for spheres, it is given by $B = 1.25 \cdot \left(\frac{1-\varepsilon}{\varepsilon}\right)^{\frac{10}{9}}$

ϕ = Contact factor $\phi = 1$ when there is complete contact, etc,

λ_R = Thermal conductivity of packed bed owing to radiation, and it is given by

$$\lambda_R = \frac{4\epsilon\sigma T^3 x_R}{1-0.132\epsilon}$$

Where:

ϵ = Emissivity of the packed bed

$\sigma = 5.67 \times 10^{-8}\mathrm{W/(m^2 \cdot K^4)}$. (Stephan-Boltzmann constant)

T = Temperature

x_R = effective length for radiation between particles , or particle diameter (pebble diameter).

Due to the fact that $\frac{\lambda_s}{\lambda_f} < 10^3$, the thermal conductivity contribution due to particle contact is neglected [31], thus equation 3.23 is reformulated viz:

$$\frac{\lambda_{eff}}{\lambda_f} = \left(1-\sqrt{1-\varepsilon}\right)\left(1+\frac{\varepsilon\lambda_R}{\lambda_f}\right) \tag{3.24}$$

$$+\sqrt{1-\varepsilon}\left\{\frac{2}{1-\frac{B\lambda_f}{\lambda_s}}\left(\frac{B}{\left(1-\frac{B\lambda_f}{\lambda_s}\right)^2}\left(1-\frac{\lambda_f}{\lambda_s}\right)ln\frac{\lambda_s}{B\lambda_f}-\frac{B+1}{2}-\frac{B-1}{1-\frac{B\lambda_f}{\lambda_s}}\right)+\frac{\lambda_R}{\lambda_f}\right\}$$

The next step entailed the calculation of the effective stagnant thermal conductivity of the bed which represents the thermal conductivity for solely conduction in a stagnated porous media. This had been captured by Zehner and Schlunder and it is given by:

$$\frac{\lambda_{eff}^0}{\lambda_f} = 1-\sqrt{1-\varepsilon}+\frac{2\cdot\sqrt{1-\varepsilon}}{1-\frac{\lambda_f}{\lambda_s}\cdot B}\cdot\left[\frac{\left(1-\frac{\lambda_f}{\lambda_s}\right)\cdot B}{\left(1-\frac{\lambda_f}{\lambda_s}B\right)^2}\cdot ln\left(\frac{\lambda_s}{B\cdot\lambda_f}\right)-\frac{B+1}{2}-\frac{B-1}{1-\frac{\lambda_f}{\lambda_s}B}\right] \tag{3.25}$$

After this, the part of the effective thermal conductivity attributed to just the radiation term was found by subtracting the effective thermal conductivity from the effective stagnant thermal conductivity as shown viz:

$$\lambda_{eff}^R = \lambda_{eff} - \lambda_{eff}^0 \tag{3.26}$$

Next, the solid and fluid effective stagnant thermal conductivity were computed from the effective stagnant thermal conductivity of the PBTES as a function of the tortuosity of the bed as shown below:

$$f = \frac{\left(\lambda_{eff,f}^0+\lambda_{eff,s}^0\right)-\varepsilon\cdot\lambda_f-(1-\varepsilon)\cdot\lambda_s}{\lambda_f-\lambda_s} \cong \frac{\lambda_{eff}^0-\varepsilon\cdot\lambda_f-(1-\varepsilon)\cdot\lambda_s}{\lambda_f-\lambda_s} \tag{3.27}$$

And finally, the effective solid and fluid thermal conductivity were calculated respectively as shown below. λ_{mix} is the contribution to the fluid conductivity when the fluid is circulating. However, since the mixing contribution of fluids is normally artificially incorporated in the fluid/solid heat transfer coefficient, it is normally neglected in many numerical models [31] and was neglected in the formulation of this model.

$$\lambda_{eff,f} \cong \left[\varepsilon \cdot \lambda_f + f \cdot \lambda_f\right] + \lambda_{mix} \tag{3.28}$$

$$\lambda_{eff,s} \cong [(1-\varepsilon) \cdot \lambda_s - f \cdot \lambda_s] + \lambda_{eff}^{R} \tag{3.29}$$

3.3.3. Temperature dependent solid thermophysical properties

As part of the improvements to the previous model, the thermophysical properties of the solid, mainly: the thermal conductivity and the specific heat capacity, were modelled as a function of temperature, to make the model more accurate. This was done by putting the temperature dependent data as an input for the model. In other words, the data source to be used for each material would have to be sourced from external standard references. This is in contrast to the thermophysical properties of the fluid which are sourced from Cantera. However, this seemed to be the only alternative, since there is no known open-source database for temperature dependent thermophysical properties of a variety of solids at the moment.

3.3.4. Pressure losses and pressure dependent flow properties

The importance of the inclusion of pressure drops and pressure dependent flow properties cannot be over emphasized in a model that is required to accurately simulate a PBTES. Despite the fact that pressure changes impact the flow properties, the pressure loss information, which is necessary to predict flow configuration designs would be very important for the incorporation of PBTES in any kind of process. The pressure drops in a porous medium like that of the packed bed storage has been properly formulated by Ergun et al [26] as captured by many authors such as Ortega et al [6] viz:

$$\frac{\Delta P}{H} = \frac{150\mu}{{d_p}^2}\frac{(1-\varepsilon)^2}{\varepsilon^3}u_\infty + \frac{1.75\rho_f}{d_p}\frac{(1-\varepsilon)}{\varepsilon^3}{u_\infty}^2 \tag{3.30}$$

At a time instant 't', the pressure at each spatial node was recalculated using the pressure from the previous node and the calculated pressure drop of the fluid, incurred during its movement from the previous spatial node to the node understudied. The pressure drop was computed as a function of the properties from the previous node (see Figure 3.3). The new pressure of the spatial node was then used to compute the velocity at that node (see equation 3.13) to fulfil the continuity equation, and the velocity was used in the energy equation to compute the temperature profiles.

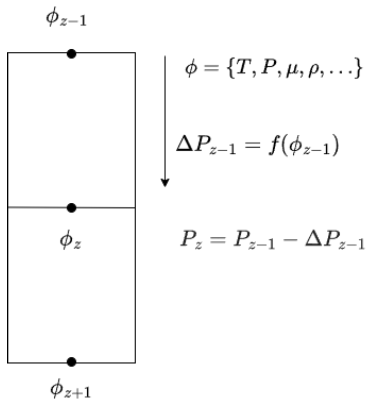

Figure 3.3: Formulation for incorporation of pressure losses

3.3.5. Correction for higher Biot numbers (Larger Pebbles)

When larger pebbles are used in a PBTES, there is a tendency for $Bi > 0.1$, and as such, it may become unrealistic to neglect the thermal gradients within the solid particles. Since the improved model is to be used to test run cases, it became imperative to include a methodology to cater for these cases. However, a robust consideration of the thermal gradients would lead to much higher model complexities, thus, a simpler method was employed as shown by Trevisan et al [8] who used the method proposed by Xu et al [16]. This approach involved the modification of the convective heat transfer co-efficient to an adjusted value as a correction factor for $Bi > 0.1$ as shown viz:

$$\frac{1}{h^*} = \frac{1}{h} + \frac{D_p}{10 \cdot \lambda_s} \tag{3.31}$$

Where h^* is the adjusted convective heat transfer coefficient.

Despite the fact that this method may not be as accurate as the acute computation of the actual thermal gradient, it is a good approximation of a correction factor for cases with non-negligible solid particle thermal gradient [16], thus it was implemented in the improved model.

3.3.6. Consideration of heat losses from the PBTES

The previously existing model did not actively consider heat losses in its formulation, and this is a huge draw back because in reality, there would almost certainly be energy losses from the PBTES to the environment in terms of heat losses, irrespective of the kind of insulating material used. Thus, this underscored the importance of modelling the energy losses in the improved model as a way of creating a more realistic model. The consideration of the heat losses from the environment involved adding a heat loss term to the fluid equation [3][6], as shown viz:

$$\varepsilon\left(\rho c_p\right)_f\left(\frac{\partial T_f}{\partial t}\right)+\left(\rho c_p\right)_f\left(u_f\frac{\partial T_f}{\partial z}\right)=\ \varepsilon\frac{\partial}{\partial z}\left(\lambda_f\frac{\partial T_f}{\partial z}\right)+ha_{sv}\left(T_s-T_f\right)+U_{loss}a_w\left(T_{ambient}-T_f\right) \qquad 3.32$$

U_{loss} is given by:

$$U_{loss}=\frac{1}{\frac{1}{h_w}+\frac{d_t}{2}\sum_{j=1}^{n_{ins}}\frac{1}{\lambda_j}ln\frac{d_{j+1}}{d_j}+\frac{d_t}{d_{ext}}\frac{1}{h_{ext}}} \qquad 3.33$$

And if there is only one insulation cover, then U_{loss} becomes:

$$U_{loss}=\frac{1}{\frac{1}{h_w}+\frac{d_t}{2\lambda_{ins}}ln\left(\frac{d_{ext}}{d_t}\right)+\frac{d_t}{d_{ext}}\frac{1}{h_{ext}}} \qquad 3.34$$

However, if the PBTES is not cylindrical as in a non-circular-base prism, U_{loss} would be written as:

$$U_{loss}=\frac{1}{\frac{1}{h_w}+\frac{\Delta x_{th}}{\lambda_{ins}}+\frac{1}{h_{ext}}} \qquad 3.35$$

Where:

d_t = diameter of inside TES tube section.

d_{ext} = external diameter of TES exposed to the surroundings.

Δx_{th} = Insulation wall thickness

a_w = wall surface area per unit bed volume

λ_{ins} = Thermal Conductivity of insulation.

λ_j = Thermal Conductivity of jth layer or insulation.

h_w = heat transfer coefficient of wall, and it is given by the following based on recommendations given by Beek [33]

$$h_w=\left(\frac{\lambda_f}{D_p}\right)\left(0.203Re^{\frac{1}{3}}Pr^{\frac{1}{3}}+0.220Re^{0.8}Pr^{0.4}\right)$$

h_{ext} = heat transfer co-efficient of external surroundings, and it is given by the correlation below used by Ortega et al [6] for free convection in vertical plates.

$$Nu_H = \frac{h_{ext}H}{\lambda_f} = 0.6 + \frac{0.387{Ra_H}^{1/6}}{\left[1+\left(\frac{0.492}{Pr}\right)^{9/16}\right]^{8/27}}$$

It is important to note that the expression above for the Nusselt number is only valid for vertical cylindrical walls when

$$\frac{d_{ext}}{H} \geq \frac{35}{Gr_H^{0.25}}$$

Where:

Gr_H = Grashof's number

Ra_H = Rayleigh's number

For the purpose of simplicity, U_{loss} was included in the algorithm as an already computed input to the model which the user is to supply. This is because of the complexities surrounding its computation in the face of different possible shape configurations, which would be quite far reaching to capture for a general 1D model within the time constraint of this thesis.

3.3.7. Code Formulation

3.3.7.1. Discretization equations and coefficients

The first step to formulating the code for the improved model involved the discretization of the modified equations or the equations of the improved model to obtain the discretization coefficients. The same discretization approach as the pre-existing model was used for the spatial discretization while the implicit time integration scheme as described in section 3.3.1 was used for the temporal discretization as shown below in the general discretization equations. It is important to note the variables with the super index 'o' represent previous time step variables and those without a super index are current time step variables.

$$\frac{T_{s,z} - {T_{s,z}}^o}{\Delta t} = \frac{\alpha_{s,z}\left(T_{s,z+1} - 2T_{s,z} + T_{s,z-1}\right)}{\Delta z^2} + \beta_{s,z}\left(T_{f,z} - T_{s,z}\right) \quad 3.36$$

$$\frac{T_{f,z} - T_{f,z}{}^{o}}{\Delta t} = \frac{u_{f,z}}{\varepsilon \Delta z}\left(T_{f,z-1} - T_{f,z}\right) + \frac{\alpha_{f,z}\left(T_{f,z+1} - 2T_{f,z} + T_{f,z-1}\right)}{\Delta z^2} + \beta_{f,z}\left(T_{s,z} - T_{f,z}\right) + \gamma_{f,z}\left(T_{ambient} - T_{f,z}\right) \tag{3.37}$$

Where

$$\gamma_{f,z} = \frac{U_{loss} a_{\mathrm{w}}}{\varepsilon(\rho c_{\mathrm{p}})_{f,z}}$$

The discretization coefficients were obtained for the co-current configuration as described in Figure 3.1, and they could be seen thus:

For solids (pebbles):

Internal nodes $(\mathbf{0} < \mathbf{z} < \mathbf{nz} - \mathbf{1})$

From equation 3.36

$$\frac{T_{s,z} - T_{s,z}{}^{o}}{\Delta t} = \frac{\alpha_{s,z}\left(T_{s,z+1} - 2T_{s,z} + T_{s,z-1}\right)}{\Delta z^2} + \beta_{s,z}\left(T_{f,z} - T_{s,z}\right)$$

Rearranging this gives

$$\left(-\frac{\alpha_{s,z}\Delta t}{\Delta z^2}\right) T_{s,z-1} + \left(1 + \frac{2\alpha_{s,z}\Delta t}{\Delta z^2} + \beta_{s,z}\Delta t\right) T_{s,z} + \left(-\frac{\alpha_{s,z}\Delta t}{\Delta z^2}\right) T_{s,z+1} + \left(-\beta_{s,z}\Delta t\right) T_{f,z} = T_{s,z}{}^{o}$$

Introducing discretization coefficients:

$$\boldsymbol{a_{N_s,z} T_{s,z-1} + a_{P_s,z} T_{s,z} + a_{S_s,z} T_{s,z+1} + b_{P_s,z} T_{f,z} = T_{s,z}{}^{o}} \tag{3.38}$$

Where:

$$a_{N_s,z} = a_{S_s,z} = -\frac{\alpha_{s,z}\Delta t}{\Delta z^2}$$

$$a_{P_s,z} = 1 + \frac{2\alpha_{s,z}\Delta t}{\Delta z^2} + \beta_{s,z}\Delta t$$

$$b_{P_s,z} = -\beta_{s,z}\Delta t$$

Boundary node $(\mathbf{z} = \mathbf{0})$

From equation 3.36,

$$\frac{T_{s,0} - T_{s,0}{}^{o}}{\Delta t} = \frac{\alpha_{s,0}\left(T_{s,1} - T_{s,0}\right)}{\Delta z^2} + \beta_{s,0}\left(T_{f,0} - T_{s,0}\right)$$

Rearranging the equation gives:

$$(1 + \frac{\alpha_{s,0}\Delta t}{\Delta z^2} + \beta_{s,0}\Delta t)\, T_{s,0} + \left(-\frac{\alpha_{s,0}\Delta t}{\Delta z^2}\right) T_{s,1} + (-\beta_{s,0}\Delta t) T_{f,0} = T_{s,0}{}^{o}$$

Introducing discretization coefficients gives

$$\boldsymbol{a_{P_s,0} T_{s,0} + a_{S_s,0} T_{s,1} + b_{P_s,0} T_{f,0} \;=\; T_{s,0}{}^{o}} \qquad 3.39$$

Where:

$a_{S_s,0} = -\frac{\alpha_{s,0}\Delta t}{\Delta z^2}$

$a_{P_s,0} = 1 + \frac{\alpha_{s,0}\Delta t}{\Delta z^2} + \beta_{s,0}\Delta t$

$b_{P_s,0} = -\beta_{s,0}\Delta t$

Boundary node **($\mathbf{z = nz - 1}$)**

From equation 3.36,

$$\frac{T_{s,nz-1} - T_{s,nz-1}{}^{o}}{\Delta t} = \frac{\alpha_{s,nz-1}\left(T_{s,nz-2} - T_{s,nz-1}\right)}{\Delta z^2} + \beta_{s,nz-1}\left(T_{f,nz-1} - T_{s,nz-1}\right)$$

Rearranging the equation gives,

$$\left(-\frac{\alpha_{s,nz-1}\Delta t}{\Delta z^2}\right) T_{s,nz-2} + (1 + \frac{\alpha_{s,nz-1}\Delta t}{\Delta z^2} + \beta_{s,nz-1}\Delta t)\, T_{s,nz-1} + \left(-\beta_{s,nz-1}\Delta t\right) T_{f,nz-1} = T_{s,nz-1}{}^{o}$$

Introducing the discretization coefficients gives:

$$\boldsymbol{a_{N_s,nz-1} T_{s,nz-2} + a_{P_s,nz-1} T_{s,nz-1} + b_{P_s,nz-1} T_{f,nz-1} \;=\; T_{s,nz-1}{}^{o}} \qquad 3.40$$

Where:

$a_{N_s,nz-1} = -\frac{\alpha_{s,nz-1}\Delta t}{\Delta z^2}$

$a_{P_s,nz-1} = 1 + \frac{\alpha_{s,nz-1}\Delta t}{\Delta z^2} + \beta_{s,nz-1}\Delta t$

$b_{P_s,nz-1} = -\beta_{s,nz-1}\Delta t$

For fluids (HTFs):

Internal nodes **($\mathbf{0 < z < nz - 1}$)**

From equation 3.37

$$\frac{T_{f,z} - T_{f,z}{}^{o}}{\Delta t} = \frac{u_{f,z}}{\varepsilon \Delta z}\left(T_{f,z-1} - T_{f,z}\right) + \frac{\alpha_{f,z}\left(T_{f,z+1} - 2T_{f,z} + T_{f,z-1}\right)}{\Delta z^2} + \beta_{f,z}\left(T_{s,z} - T_{f,z}\right) + \gamma_{f,z}\left(T_{ambient} - T_{f,z}\right)$$

Re-arranging the equation,

$$\left(-\frac{\alpha_{f,z}\Delta t}{\Delta z^2} - \frac{u_f \Delta t}{\varepsilon \Delta z}\right) T_{f,z-1} + \left(1 + \frac{2\alpha_{f,z}\Delta t}{\Delta z^2} + \frac{u_f \Delta t}{\varepsilon \Delta z} + \beta_{f,z}\Delta t + \gamma_{f,z}\Delta t\right) T_{f,z} + \left(-\frac{\alpha_{f,z}\Delta t}{\Delta z^2}\right) T_{f,z+1} + \left(-\beta_{f,z}\Delta t\right) T_{s,z} = T_{f,z}{}^{o} + \gamma_{f,z}\Delta t T_{ambient}$$

Introducing discretization coefficients gives:

$$\boldsymbol{a_{N_{f,z}} T_{f,z-1} + a_{P_{f,z}} T_{f,z} + a_{S_{f,z}} T_{f,z+1} + b_{P_{f,z}} T_{s,z} = T_{f,z}{}^{o} + D} \qquad 3.41$$

Where:

$$a_{N_{f,z}} = -\frac{\alpha_{f,z}\Delta t}{\Delta z^2} - \frac{u_f \Delta t}{\varepsilon \Delta z}$$

$$a_{S_{f,z}} = -\frac{\alpha_{f,z}\Delta t}{\Delta z^2}$$

$$a_{P_{f,z}} = 1 + \frac{2\alpha_{f,z}\Delta t}{\Delta z^2} + \frac{u_f \Delta t}{\varepsilon \Delta z} + \beta_{f,z}\Delta t + \gamma_f \Delta t$$

$$b_{P_{f,z}} = -\beta_{f,z}\Delta t$$

$$D = \gamma_{f,z}\Delta t T_{ambient}$$

Boundary node **($\mathbf{z = 0}$)**

From equation 3.37, using the charging case as the case study,

$$\frac{T_{f,0} - T_{f,0}{}^{o}}{\Delta t} = \frac{u_{f,0}}{\varepsilon \Delta z}\left(T_{fumes,in} - T_{f,0}\right) + \frac{\alpha_{f,0}\left(T_{f,1} - 2T_{f,0} + T_{fumes,\ in}\right)}{\Delta z^2} + \beta_{f,0}\left(T_{s,0} - T_{f,0}\right) + \gamma_{f,0}\left(T_{ambient} - T_{f,0}\right)$$

Rearranging the equation gives

$$\left(1 + \frac{2\alpha_{f,0}\Delta t}{\Delta z^2} + \frac{u_{f,0}\Delta t}{\varepsilon \Delta z} + \beta_{f,0}\Delta t + \gamma_{f,0}\Delta t\right) T_{f,0} + \left(-\frac{\alpha_{f,0}\Delta t}{\Delta z^2}\right) T_{f,1}$$

$$+\left(-\beta_{f,0}\Delta t\right) T_{s,0} = T_{f,0}{}^{o} + \left(\frac{\alpha_{f,0}\Delta t}{\Delta z^2} + \frac{u_{f,0}\Delta t}{\varepsilon \Delta z}\right) T_{fumes,in} + \gamma_{f,0}\Delta t T_{ambient}$$

Introducing discretization coefficients gives

$$\boldsymbol{a_{P_f,0}T_{f,0} + a_{S_f,0}T_{f,1} + b_{P_f,0}T_{s,0} \; = \; T_{f,0}{}^o + C + D} \qquad 3.42$$

Where:

$$a_{S_f,0} = -\frac{\alpha_{f,0}\Delta t}{\Delta z^2}$$

$$a_{P_f,0} = \; 1 + \frac{2\alpha_{f,0}\Delta t}{\Delta z^2} + \frac{u_{f,0}\Delta t}{\varepsilon \Delta z} + \beta_{f,0}\Delta t \; + \; \gamma_{f,0}\Delta t$$

$$b_{P_f,0} = \; -\beta_{f,0}\Delta t$$

$$C = \left(\frac{\alpha_{f,0}\Delta t}{\Delta z^2} + \frac{u_{f,0}\Delta t}{\varepsilon \Delta z}\right) T_{fumes,in}$$

$$D = \; \gamma_{f,z}\Delta t T_{ambient}$$

Boundary node $(\mathbf{z = nz - 1})$

From equation 3.37, using the charging case as the case study,

$$\frac{T_{f,nz-1} - T_{f,nz-1}{}^o}{\Delta t} = \frac{u_{f,nz-1}}{\varepsilon \Delta z}\left(T_{f,nz-2} - \; T_{f,nz-1}\right) + \frac{\alpha_{f,nz-1}\left(T_{f,nz-2} - T_{f,nz-1}\right)}{\Delta z^2} + \beta_{f,nz-1}\big(T_{s,nz-1} - T_{f,nz-1}\big) \; + \; \gamma_{f,nz-1}\left(T_{ambient} - T_{f,nz-1}\right)$$

Rearranging the equation gives:

$$\left(-\frac{u_{f,nz-1}\Delta t}{\varepsilon \Delta z} - \frac{\alpha_{f,nz-1}\Delta t}{\Delta z^2}\right) T_{f,nz-2} + \left(1 + \frac{u_{f,nz-1}\Delta t}{\varepsilon \Delta z} + \frac{\alpha_{f,nz-1}\Delta t}{\Delta z^2} + \beta_{f,nz-1}\Delta t\right) T_{f,nz-1} + \left(-\beta_{f,nz-1}\Delta t\right) T_{s,nz-1} = \; T_{f,nz-1}{}^o + \; \gamma_{f,nz-1}\Delta t T_{ambient}$$

Introducing the discretization coefficients gives:

$$\boldsymbol{a_{N_f,nz-1}T_{f,nz-2} + a_{P_f,nz-1}T_{f,nz-1} + b_{P_f,nz-1}T_{s,nz-1} \; = \; T_{f,nz-1}{}^o + D} \qquad 3.43$$

Where:

$$a_{N_f,nz-1} = \; -\frac{u_{f,nz-1}\Delta t}{\varepsilon \Delta z} - \frac{\alpha_{f,nz-1}\Delta t}{\Delta z^2}$$

$$a_{P_f,nz-1} = \; 1 + \frac{u_{f,nz-1}\Delta t}{\varepsilon \Delta z} + \frac{\alpha_{f,nz-1}\Delta t}{\Delta z^2} + \; \beta_{f,nz-1}\Delta t$$

$$b_{P_f,nz-1} = \; -\beta_{f,nz-1}\Delta t$$

$$D = \; \gamma_{f,z}\Delta t T_{ambient}$$

3.3.7.2. Matrix Formulation

A matrix-related computational arrangement was selected to solve the discretization equations for a number of grids, as shown in equation 3.38 to 3.43, hence, it was expedient to put the equations in a matrix form. It was not practical to solve the fluid and solid equations separately with two matrix equations due to the fact that the PDEs are coupled via the convection term such that the solid temperature, is used in the fluid model and the fluid temperature is used in the solid model. In other words, to solve for the fluid temperatures, the result of the solid model was needed, and to also solve the solid model, the result of the fluid temperature was needed. Thus, a methodology similar to that of Tusek et al [34] was used, which employed a one matrix equation to solve a system of two PDEs for a one-dimensional numerical model to study the operation of an active magnetic regenerator (AMR).

To create this matrix, the equations had to be arranged such that the unknowns were on the left-hand side of the equation and the known parameters were at the right-hand side of the equation, factorizing terms to have a system of equation with distinct unknown temperatures multiplied by an underlying coefficient, as this enabled the conversion to a matrix equation. Since the fluid and solid domains were divided into nz nodes each ranging from node 0 to node $nz - 1$, the matrix was one with size $2nz \times 2nz$ written such that the top nz rows of the matrix contained the fluid equations and the bottom nz rows held the solid (pebble) equations. Doing this while upholding the matrix multiplication rules led to the first nz columns of the matrix holding the discretization coefficients of unknown fluid temperatures and the last nz columns of the matrix, containing the discretization coefficients of unknown solid temperatures. The first half of the unknown temperature vector contained the unknown fluid temperatures, and the bottom half contained the unknown solid or pebble temperatures. The boundary condition equations for the fluid and pebbles were placed at the top and bottom of the first and second half matrix partitions respectively as seen below. Executing the corroborated strategy into equations 3.38 to 3.43 gave the matrix arrangement captured below:

$$\left[\begin{array}{ccccc|ccccc}
a_{P_f,0} & a_{S_f,0} & 0 & 0 & 0 & b_{P_f,0} & 0 & 0 & 0 & 0 \\
a_{N_f,z} & a_{P_f,z} & a_{S_f,z} & 0 & 0 & 0 & b_{P_f,z} & 0 & 0 & 0 \\
0 & . & . & . & 0 & 0 & 0 & . & 0 & 0 \\
0 & 0 & . & . & . & 0 & 0 & 0 & . & 0 \\
0 & 0 & 0 & a_{N_f,nz-1} & a_{P_f,nz-1} & 0 & 0 & 0 & 0 & b_{P_f,nz-1} \\
\hline
b_{P_s,0} & 0 & 0 & 0 & 0 & a_{P_s,0} & a_{S_s,0} & 0 & 0 & 0 \\
0 & b_{P_s,z} & 0 & 0 & 0 & a_{N_s,z} & a_{P_s,z} & a_{S_s,z} & 0 & 0 \\
0 & 0 & . & 0 & 0 & 0 & . & . & . & 0 \\
0 & 0 & 0 & . & 0 & 0 & 0 & . & . & . \\
0 & 0 & 0 & 0 & b_{P_s,nz-1} & 0 & 0 & 0 & a_{N_s,nz-1} & a_{P_s,nz-1}
\end{array}\right]
\begin{bmatrix} T_{f,0} \\ T_{f,z} \\ . \\ T_{f,nz-2} \\ T_{f,nz-1} \\ T_{s,0} \\ T_{s,z} \\ . \\ T_{s,nz-2} \\ T_{s,nz-1} \end{bmatrix}
=
\begin{bmatrix} T_{f,0}{}^{o} + C + D \\ T_{f,z}{}^{o} + D \\ . \\ . \\ T_{f,nz-1}{}^{o} + D \\ T_{s,0}{}^{o} \\ T_{s,z}{}^{o} \\ . \\ . \\ T_{s,nz-1}{}^{o} \end{bmatrix} \tag{3.44}$$

The $2nz \times 2nz$ matrix was constructed for nz number of nodes such that:

For Node $\boldsymbol{z = 0}$ ***to*** $\boldsymbol{nz - 1}$**, where applicable,**

$a_{N_f,z} = A[z,\ z - 1]$

$a_{P_f,z} = A[z,\ z]$

$a_{S_f,z} = A[z,\ z + 1]$

$b_{P_f,z} = A[z,\ nz + z]$

$a_{N_s,z} = A[nz + z,\ nz + (z - 1)]$

$a_{P_s,z} = A[nz + z,\ nz + z]$

$a_{S_s,z} = A[nz + z,\ nz + (z + 1)]$

$b_{P_s,z} = A[\ nz + z,\ z\ ]$

Thus, the system of equations became easily reduced to the matrix equation format below:

$$[A]\ [\vec{T}] = [\vec{B}] \tag{3.45}$$

3.3.7.3. Matrix Solver

The matrix 'A' in equation 3.44 and 3.45, created as a result of the implicitly discretized continuous solid heat equation for a packed bed thermal energy storage, is a special type of Penta-diagonal matrix called an 'Outrigger Matrix'. An Outrigger matrix is one whose zero entries are confined within the main diagonals and the outer bands [35], and such matrices are widely known to mandatorily require the use of iteration solution schemes such as Jacobi and Gauss–Seidel [36]. Nevertheless, to solve this matrix during each iteration, a solver from NumPy - a python library, was used. It is called the NumPy Linear Algebra Function written as “numpy.linalg.solve” which computes matrix equation solutions using the LAPACK (Linear Algebra Package) routine “_gesv” [37]. The name “_gesv” stands for ‘generalized equation solver with LU factorization” and it solves a linear system of equations, giving exact solutions as long as the coefficient Matrix of the formation is a square whose rows are linearly independent (full rank matrix). Given a square coefficient matrix A and a right-hand side vector x such that $Ax = b$, the routine obtains the exact solution vector x by performing a Gaussian elimination with partial pivoting on matrix A often called ‘LU factorization’. LU factorization entails the decomposition of the coefficient matrix A into a product of two matrices $A = LU$ such that L is a lower triangular matrix with ones on the diagonal and U is an upper triangular matrix. Once LU factorization is complete, the routine solves the system using forward and backward substitution [37].

3.3.7.4. Code Algorithm.

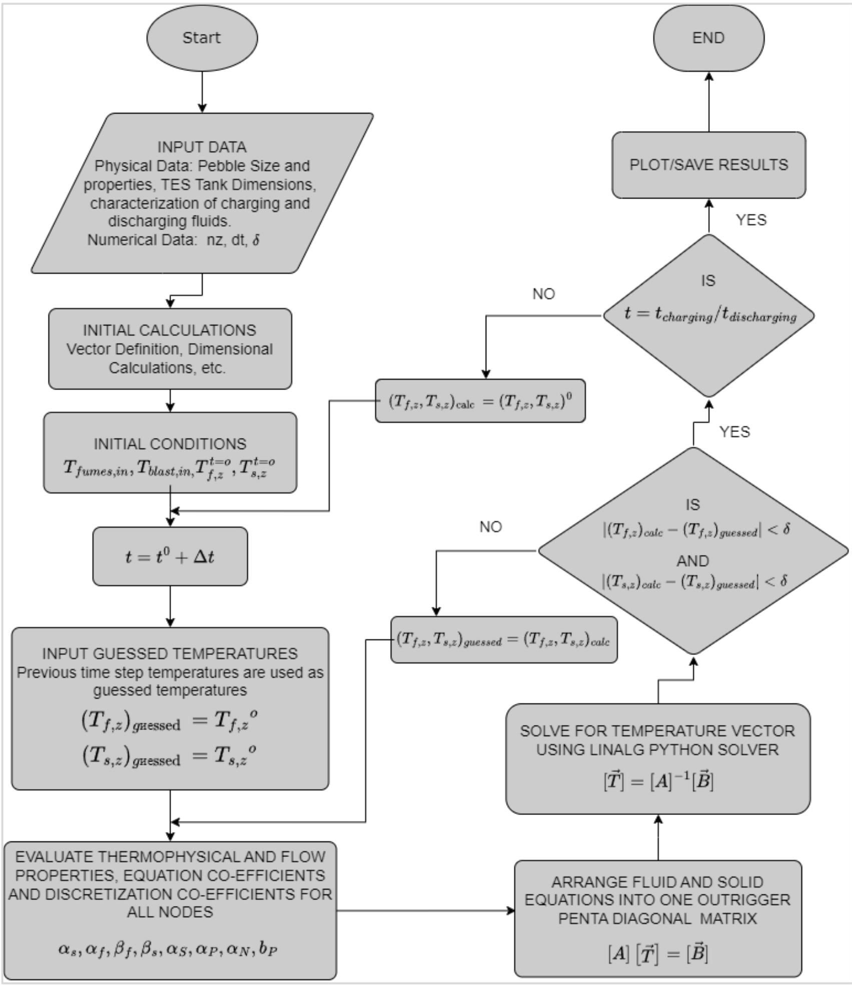

Figure 3.4: Algorithm for Improved Model

Having established the discretization equations, matrix formulation and matrix solver, the python code for the model was created using the algorithm shown in Figure 3.4. As previously hinted, the algorithm makes use of the Gauss-Siedel iterative method, which upon each iteration, resolves the model matrix equation using the matrix solver earlier described. The input values of the model were coined from a reference value case established by ArcelorMittal. For the temperature dependent variable thermophysical properties, a reference material was selected and the curves and tables of the material's thermophysical properties as a function of temperature was made available by the company to be used to test run the model. The reference case and material are properly expatiated in the subsequent chapter of this work alongside the corresponding results.

3.3.8. Counter Current configuration

As previously stated, the counter current pebble heater configuration involves charging the pebble heater from the top with a hot HTF or fumes and discharging the pebble heater from the bottom using a cool HTF or blast air. This configuration was not captured in the previous model, but it became pertinent to add it to the co-current configuration as part of the model improvements, since similar configurations are commonly seen in pebble heater usage. The addition of this configuration required that changes be made to the flow direction of the discharging phase of the configuration, since in the charging phase, the HTF would come from the top like in the co-current phase. From a general perspective, the configuration change simply warranted a modification of the velocity field vector in the general equations captured in equations 3.13.1 - 3.4, however, from the model-defined perspective, the use of the upwind scheme for the convective term discretization required the execution of an adjustment, to consider the change in the boundary conditions and in the designation of the upstream node to match the new flow direction of the HTF, and this led to the reformulation of the discretized fluid equation shown below, as well as the corresponding discretization coefficients used in the matrix .

$$\frac{T_{f,z} - T_{f,z}{}^{o}}{\Delta t} = \frac{u_{f,z}}{\varepsilon \Delta z}\left(\boldsymbol{T_{f,z+1}} - T_{f,z}\right) + \frac{\alpha_{f,z}\left(T_{f,z+1} - 2T_{f,z} + T_{f,z-1}\right)}{\Delta z^2} + \beta_{f,z}\left(T_{s,z} - T_{f,z}\right) + \gamma_{f,z}\left(T_{ambient} - T_{f,z}\right) \tag{3.46}$$

The step-by-step formulation for this is captured in Appendix A, and the matrix equation resulting from the modification was solved using the same strategy as that of the co-current case. To ensure that the model could run both configurations, two different functions were created tor the two different matrix equations, and each configuration could easily be called up by the user via a particular key input, whose nomenclature was predefined in the code.

3.4. Model Verification and Mesh Size Selection

The verification of the model involves establishing the numerical accuracy of the code or checking that the code created has correctly solved the equation that it was fed to solve, and it is an important preliminary step to confirming the accuracy of a code or model. The verification for the model was executed by performing an error check on the energy balance of the system which is basically conceptualized by the equation below.

$$Energy\ balance\ Error = Energy\ transfer\ from\ or\ to\ HTF - Energy\ stored\ in\ PBTES \pm Energy\ Losses \qquad 3.47$$

The sign beside the energy losses is positive during the discharging phase (when energy is transferred from the PBTES) and is negative during the charging phase (when energy is transferred from the HTF to the PBTES). The energy balance was executed for each time step in both the charging and discharging phase using the expanded equation format shown in equation 3.48. The energy stored in the pebble heater was computed as a sum of the energy stored by the pebbles and energy stored in the pebble heater interstices via dividing the domain into control volumes as exemplified in Figure 3.5, with the properties of each control volume computed using that of the node above it.

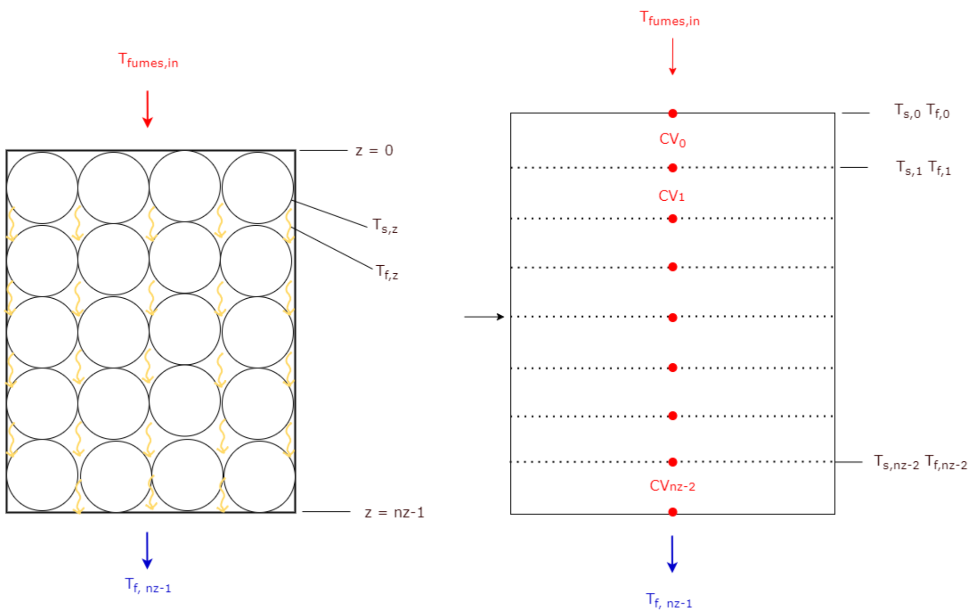

Figure 3.5: Energy Balance Formulation in charging phase

$$Energy\ Balance\ Error = \pm[\ \rho_{HTF,in}u_{HTF,in}h(T_{HTF,in}) - \rho_{HTF,out}u_{HTF,out}h(T_{HTF,out})] \mp [\sum_0^{nz-2}(1-\varepsilon)\rho_{s,z}C_{p_{s,z}}(T_{s,z} - T_{s,z}{}^{o})S_{passage}dz + \sum_0^{nz-2}\varepsilon(\rho_{f,z}h(T_{f,z}) - \rho_{f,z}{}^{o}h(T_{f,z}{}^{o}))S_{passage}dz\ ] \pm \sum_0^{nz-2}U_{loss}a_w(T_{f,z} - T_{ambient})dz\ ]S_{passage}\Delta t \qquad 3.48$$

The top operation signs across equation 3.48 were used for the charging phase and that of the bottom for the discharging phase. Also, the fluid variables at the exit node was used for the 'HTF out' properties.

The result from the energy balance error was used to determine optimum mesh sizes in both the spatial and temporal domain, and verify the code, by computing the relative energy balance percentage error as highlighted by Muske et al [38], and shown in the equation below.

$$Relative\ Energy\ Balance\ \%\ Error = \frac{Energy\ balance\ error\ value}{Energy\ Stored\ in\ PBTES} \qquad 3.49$$

The code was said to be verified if the relative energy balance percentage error was very low (< 5% as prescribed by the company for this modelling stage) and if it also decreased with a finer mesh, and the optimum mesh size was slated to be the mesh size at the region where increasing the mesh finesse leads to very little or no error percentage decrements.

3.5. Model Validation

The validation of the model involves performing a check to ensure that the model is accurately modelling the physical process or phenomenon that it was created to simulate, and it is the final step to checking the validity of the model. Model validation is often done by comparison with either the general analytical solution of the physical problem, if available or with experimental results. Due to the complexity surrounding the generation of an analytical solution for a porous medium that captures all the phenomena occurring in the real world, an experimental case was used to validate the model. The experimental case employed, was that used by Hanchen et al [39] to validate their packed bed storage model. The experimental process was carried out by Meier et al [40] who measured the temperature evolution of an axial packed bed storage. The experimental set up as seen in Figure 3.6 and consisted of a vessel made of stainless steel, whose wall was 1.5 mm thick and was insulated both internally and externally. The summary of the input data is seen in Figure 3.7 and it was keyed into the model during the validation. The data points from the experimental results were extracted from the experimental points plotted by Hanchen et al (see Figure 3.8) and they were plotted side by side with the results obtained from the numerical model. Finally, a mesh refinement plot was executed to check that the validation error decreased with the use of finer meshes.

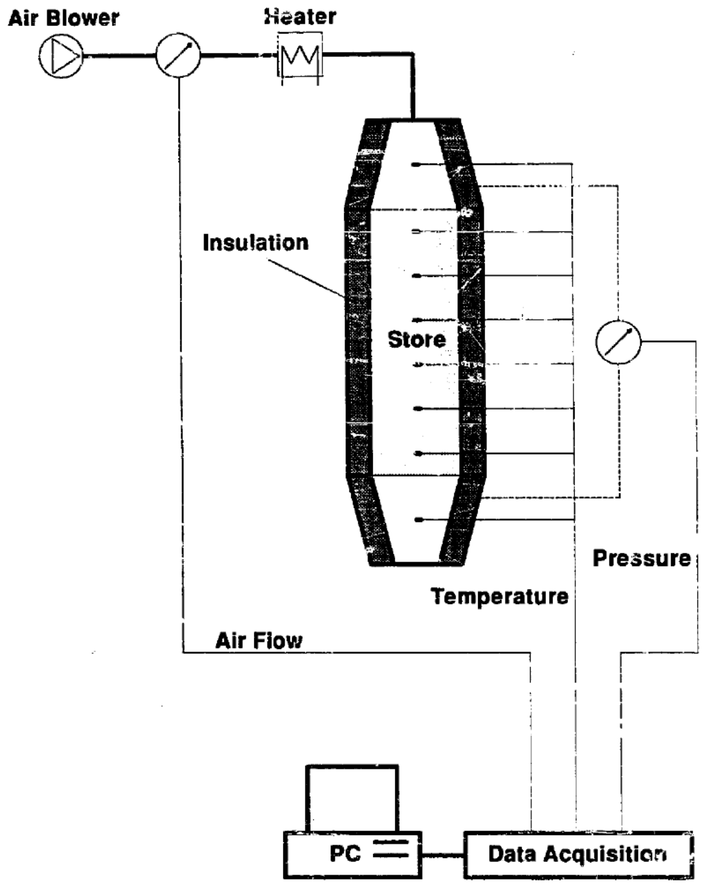

Figure 3.6: Experimental set up for case used in the model validation [40]

Parameter	Value
T_{in}	823 K
T_{inf}	293 K
G	0.225 $kg/m^2\,s$
H	1.2 m
D	0.148 m
A	0.0172 m
ε	0.4
d	0.02 m
ρ_s	2680 kg/m^3
c_s	1068 J/(kg K)
k_s	2.5 W/(m K)
U	0.678 $W/(m^2\,K)$
n	100

Figure 3.7: Summary of Input values for experimental case used in the model validation [39]

It is important to note that the wall effects present in the experiments, which were not captured by the numerical model, was accounted for by factoring into the validation input, a bypass flow rate equivalent to 15% of the total mass flowrate as recommended by

Hanchen et al [39].

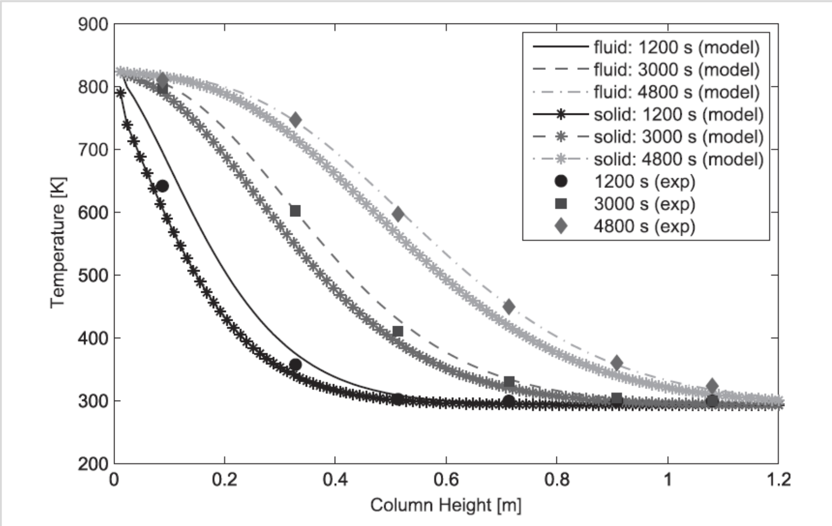

Figure 3.8: Source for experimental result data points used in Model Validation

4. Results and Discussion

4.1. Model Verification Results

The results for the verification of the model are shown in Figure 4.1, which captures the relative energy balance percentage error for mesh sizes in both the spatial and temporal dimensions.

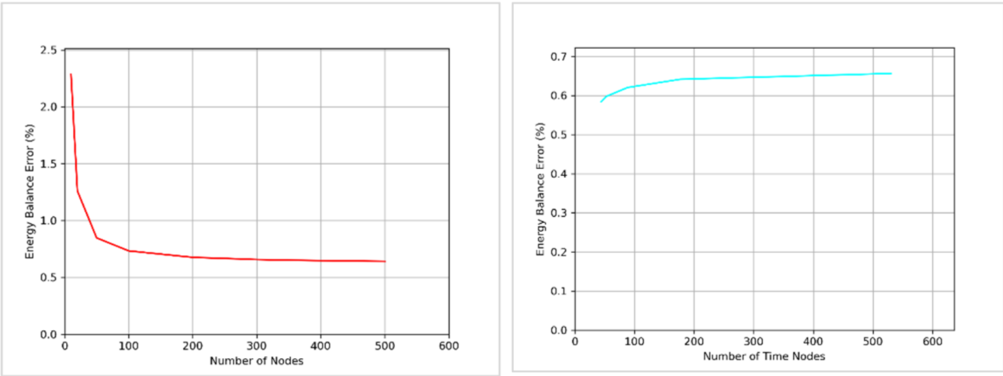

(a) (b)

Figure 4.1: Model verification results for (a) Spatial mesh (b) Temporal mesh.

For the spatial mesh, the percentage error is very low, and it reduces hyperbolically to almost zero percentage values with an increase in the number of spatial nodes, which is very acceptable, and for the temporal mesh, the percentage error is much lower, which is very acceptable, however, the error seems not to change a lot with the increase in the temporal mesh number. Additional verification exercises using the courant's number could be performed, to check the influence of the spatial and temporal meshes together, without any error influence from the other, however, this was not done because energy balance errors below 5% was deemed acceptable by the company for this modelling scope, and time resources needed to be refocused to prioritize other crucial model additions and thesis activities.

4.2. Model Validation Results

The results for the model validation are captured in Figure 4.2, and it could be clearly seen that the model results agree reasonably with the experimental results. Figure 4.2 also shows a spatial mesh refinement study capturing the validation error between the model results and the experimental results, and it is clearly seen that the error reduces with an increase in the number of meshes or nodes used, thus the model could be said to be validated.

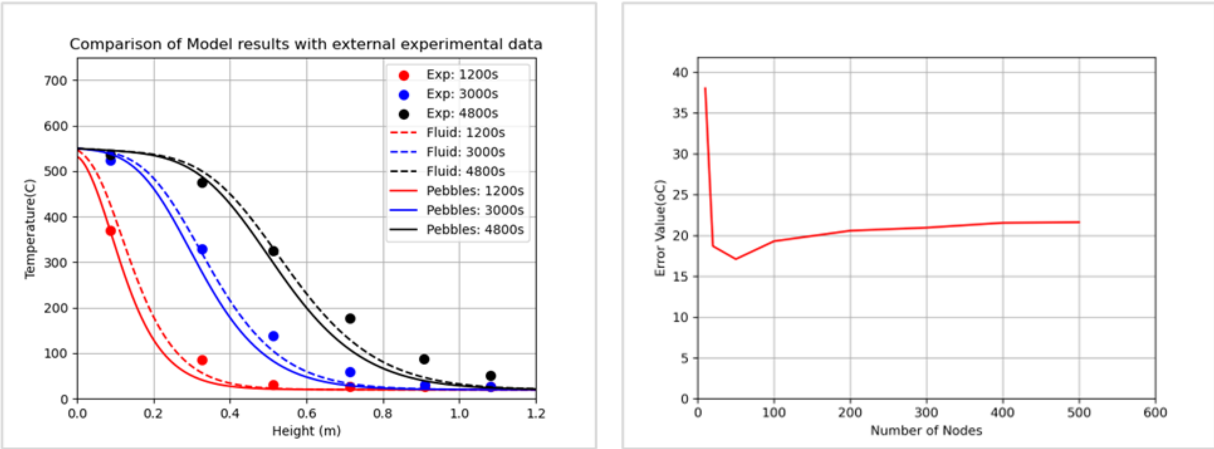

Figure 4.2: Model Validation Results

An additional investigation into the model validation was also done, and the formulation of the heat transfer co-efficient used in the model was changed to the formulation for the heat transfer used by the experimental data source, and a better model fit was obtained as well as lower validation error values as shown in Figure 4.3. This occurrence points towards the indication that the formulation of the heat transfer coefficient used, significantly affects the shape of the temperature distribution curve, and care must be taken to select formulations that best agrees with the experimentation conditions.

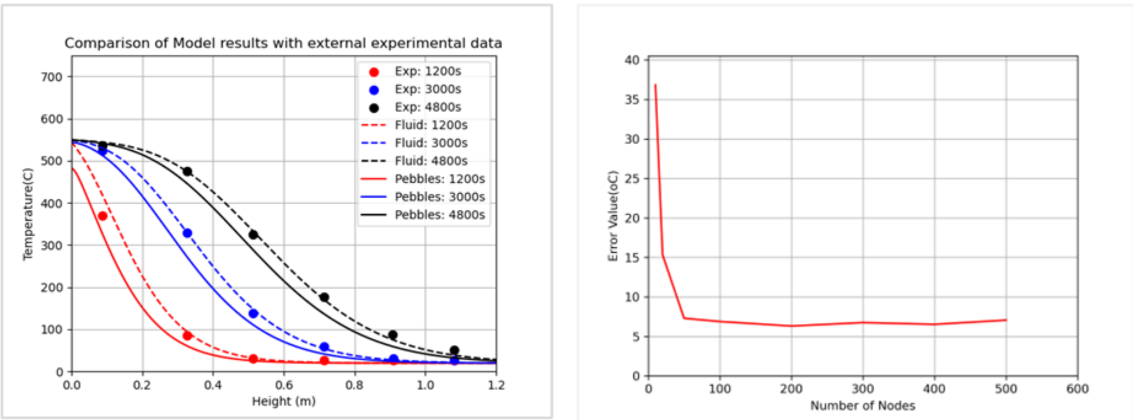

Figure 4.3: Model Validation Results using data source proposed heat transfer coefficient.

4.3. Model Results with Reference Case

After the verification and validation of the model, it was run with a reference case of input parameters provided by the company as a base for further study. The table containing the input parameters could be seen below. The reference case assumed a scenario where the PBTES is charged for a while with fumes from an arbitrary steel plant source and subsequently immediately discharged with blast air without any idling period in the co-current configuration.

Table 4.1 Reference case input values for model test

INPUT DATA	VALUES
PBTES shape	Square Cylinder
PBTES Cross Section Side	0.1m
PBTES Height	1.5m
Pebble (Particle) Diameter	6.4mm
Particle shape factor	0.9
Particle emissivity	0.55
Particle density	2350Kg/m^3
Bed Porosity	0.38
T_{fumes} / P_{fumes}	1050ºC/1atm
T_{blast} / P_{blast}	40ºC/1atm
$T_{ambient}$	20ºC
Q_V_fumes/ Q_V_blast	10.6145Nm^3/h / 13.682Nm^3/h
Charging time (with fumes)	3300s
Discharging time (with blast air)	1600s
Gauss-Seidel Iteration Residual	0.00001
Time step (dt)	10s
Number of discretization nodes (nz)	300
$T_{initial}$	40ºC

Thus, the initial temperature distribution of the bed before charging for both the solid and the fluid was set to '$T_{initial}$' and the initial temperature distribution of the bed for the discharging phase was set to be the temperature distribution of the bed just after charging. For the variable thermophysical properties of the solid, a reference material was provided by the company and the plot of its variable thermophysical properties could be seen in Figure 4.4. Also, for the sake of visualization, the effective thermal conductivities as well as its solid and fluid contributions were also plotted as a function of temperature, with a subplot to show the importance of the radiative term in the accuracy of the value of the solid effective thermal conductivity. The results of the charging and discharging phase are shown in Figure 4.5 and Figure 4.6 below at some randomly-chosen specific time interval. In the charging phase, the temperature of the PBTES in each height section rises till gets to the maximum value corresponding the temperature of the fumes that entered into the system, and a thermal front between the maximum temperature and the minimum temperature of the PBTES is created.

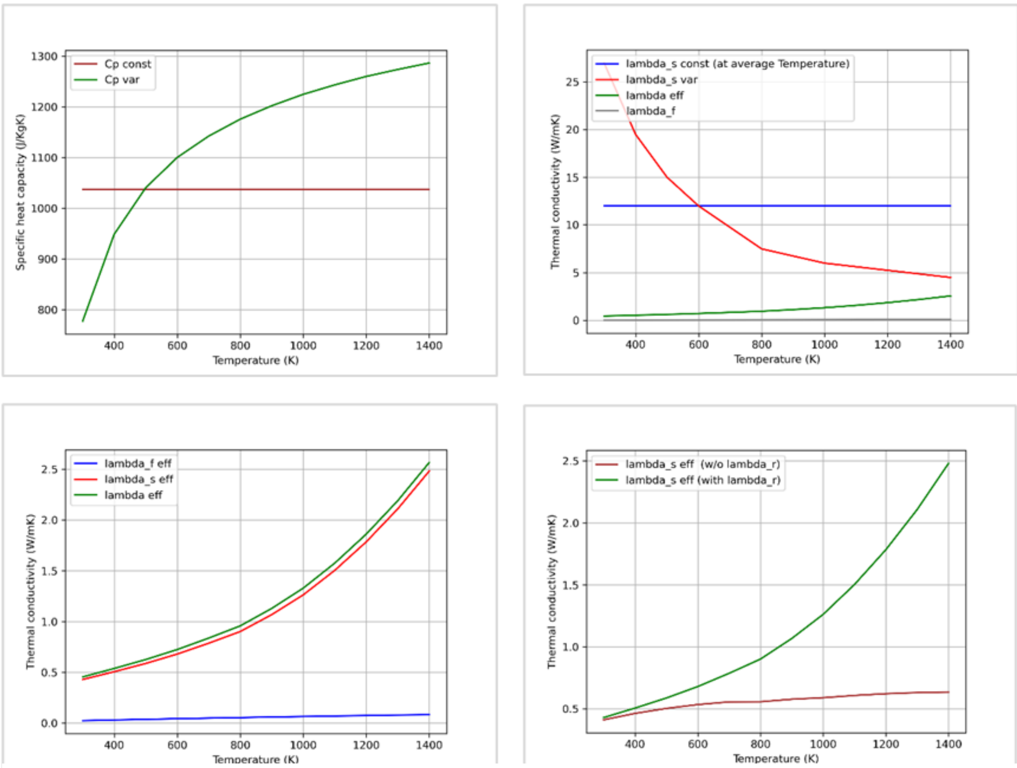

Figure 4.4: Thermophysical properties of reference material used in reference case.

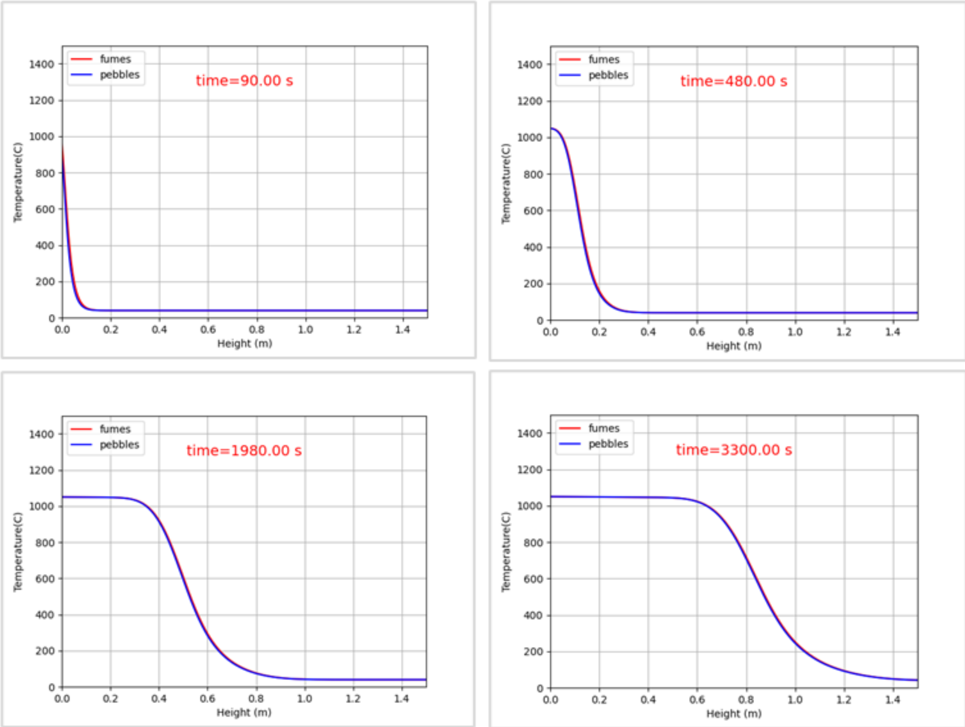

Figure 4.5: Model Results – Charging phase in Co-current configuration.

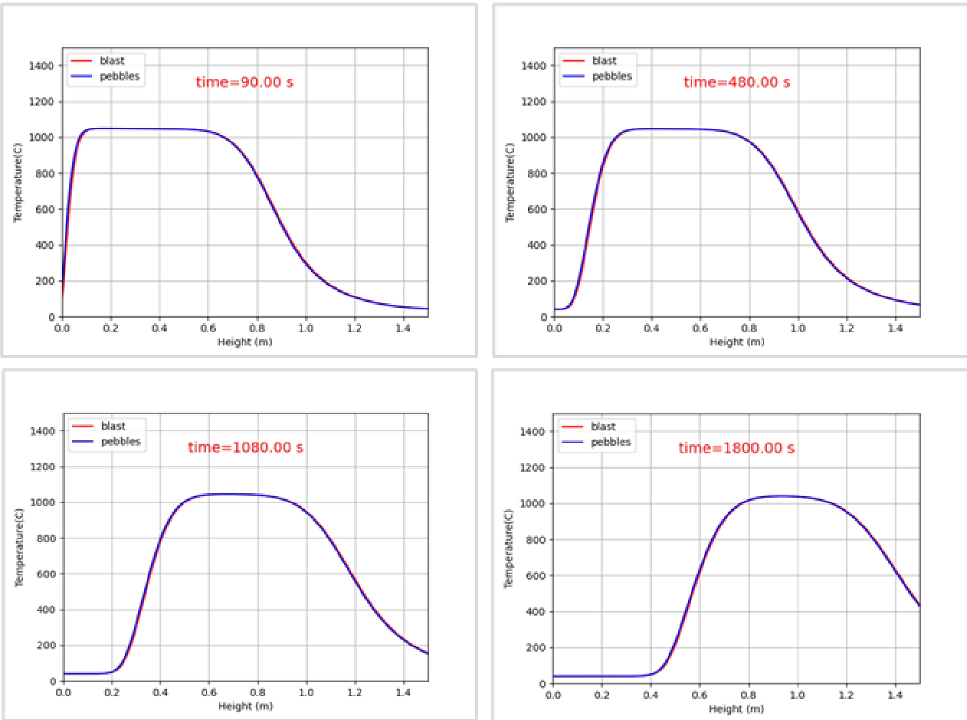

Figure 4.6: Model Results – Discharging phase in Co-current configuration.

This thermal front gradually shifts to the right with the evolution of time until the end of the charging cycle. In the discharging phase – which begins with the PBTES possessing the same temperature distribution as that obtained at the end of the charging phase, a very interesting phenomenon could be observed. Due to the co-current configuration used, the cold/discharging HTF comes into the PBTES from the top, gets heated along the PBTES, only to lose this heat again to the cold solid particles at the bottom end of the PBTES, hence, for a long period of time, the HTF exiting the end of the PBTES actually remains within the same temperature range. Thus, it shows that a co-current discharging configuration entails the HTF not being heated for an initial amount of time due to the preliminarily forced movement of energy from the top side of the PBTES to the bottom side. The result for the co-current configuration underscores the importance of the counter current configuration whose results are seen below in Figure 4.7 – where the discharging phase of the counter current configuration is shown.

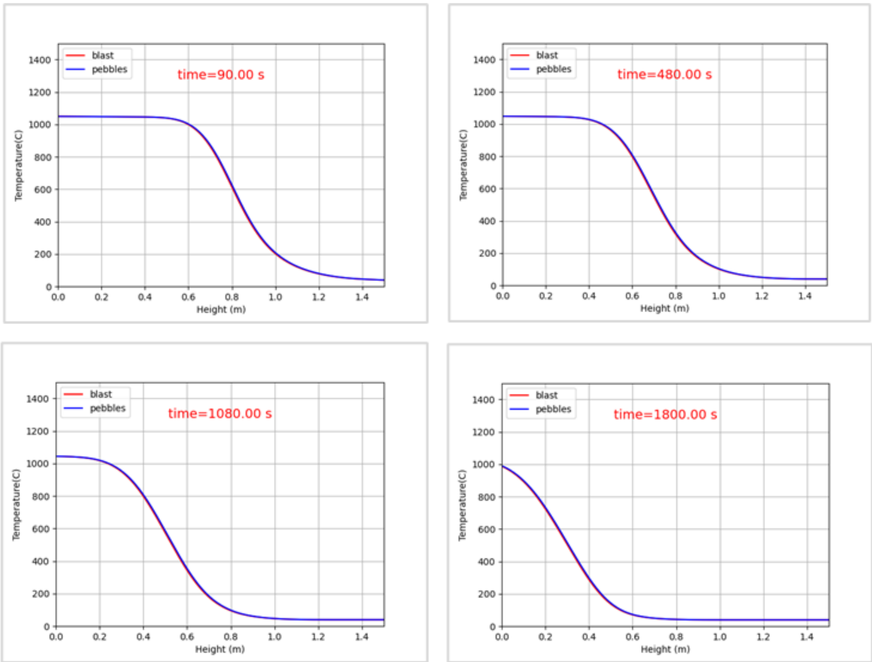

Figure 4.7: Model Results – Discharging phase in Counter current configuration.

As could be acutely observed, right from the start of the discharging in the counter current configuration, the discharging fluid leaves the PBTES at node zero, at the maximum temperature of the PBTES, and this continues till the end of the discharging time. Thus, the counter current configuration is the better configuration for discharging an already charged PBTES.

The results from the pressure drop are also plotted in Figure 4.8. The pressure profiles changed across the charging and discharging times due to the fact that the flow properties used during its computation was also a function of temperature, which changes with time. The pressure profiles at the end of the charging and discharging phase for the counter current configuration were used as a sample as shown in Figure 4.8. The pressure profile at the end of each phase was selected because it represented the maximum pressure difference within the whole cycle. The pressure drop incurred was around 43mbar for both phases which is quite expected due to the small height of the bed.

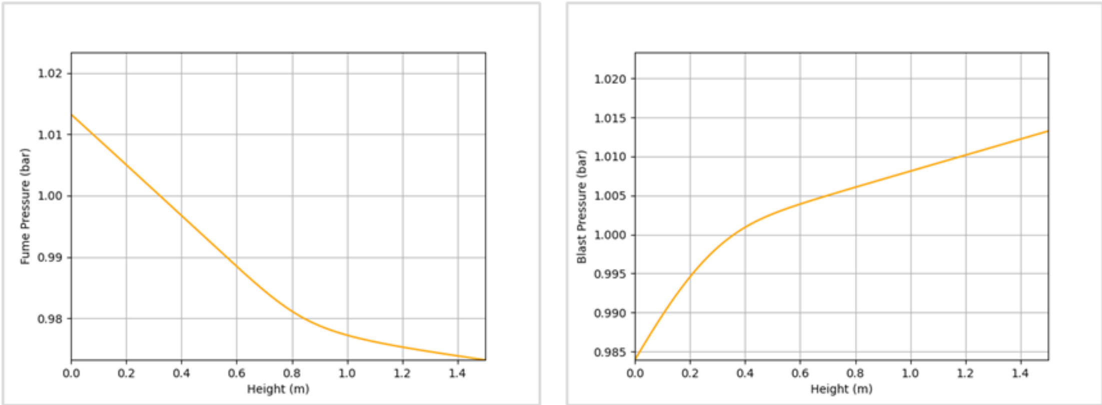

Figure 4.8: Pressure profiles at the end of charging and discharging phase

4.4. Sensitivity Analysis

As a preview to the parametric analysis for the enhancement of PBTES design decisions, a sensitivity analysis was executed to check the effect of some variables on the PBTES operation. Due to the constrain of obtaining data for the temperature dependent thermophysical properties used in the model, the sensitivity analysis was performed using percentage increments or decrements of the original variable thermophysical properties used.

4.4.1. Thermal conductivity of the solid particle.

A change in the thermal conductivity of the solids as shown in Figure 4.9 does not really affect the temperature distribution of the PBTES. This could be traced to the fact that the effective thermal conductivity is a function of not only the solid thermal conductivity, but also the fluid thermal conductivity, which is very low in the model case, thus, resulting in very little changes to the effective thermal conductivity even when the conductivity of the solids is increased.

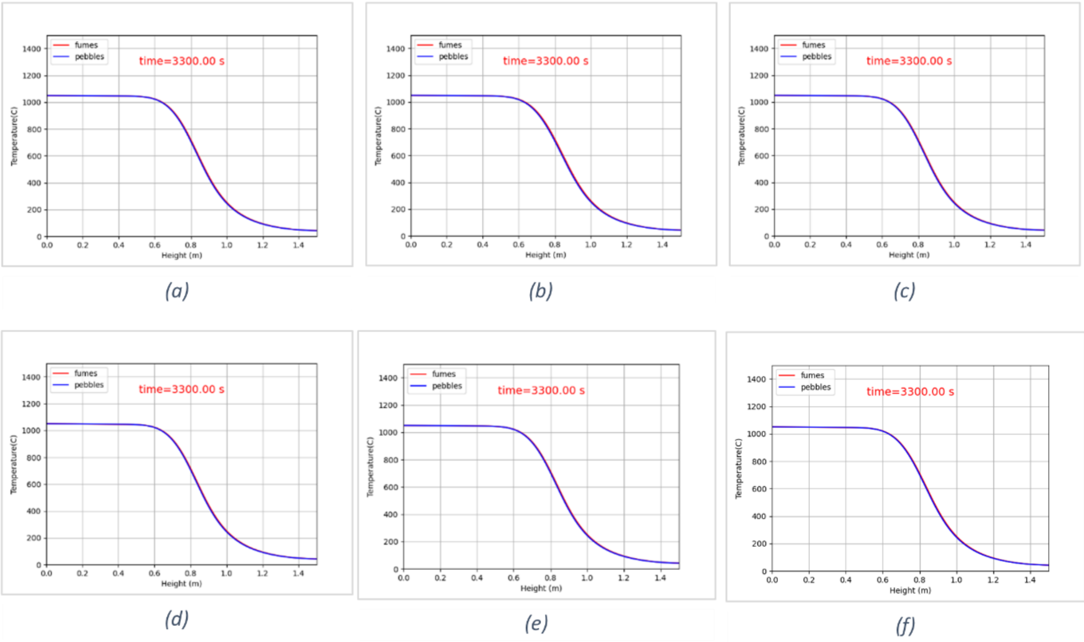

Figure 4.9: Sensitivity of λ_s (a) -50% (b) -90% (c) Original (d)+50% (e) +300% (f) +1000%

4.4.2. Specific heat capacity of the solid particle

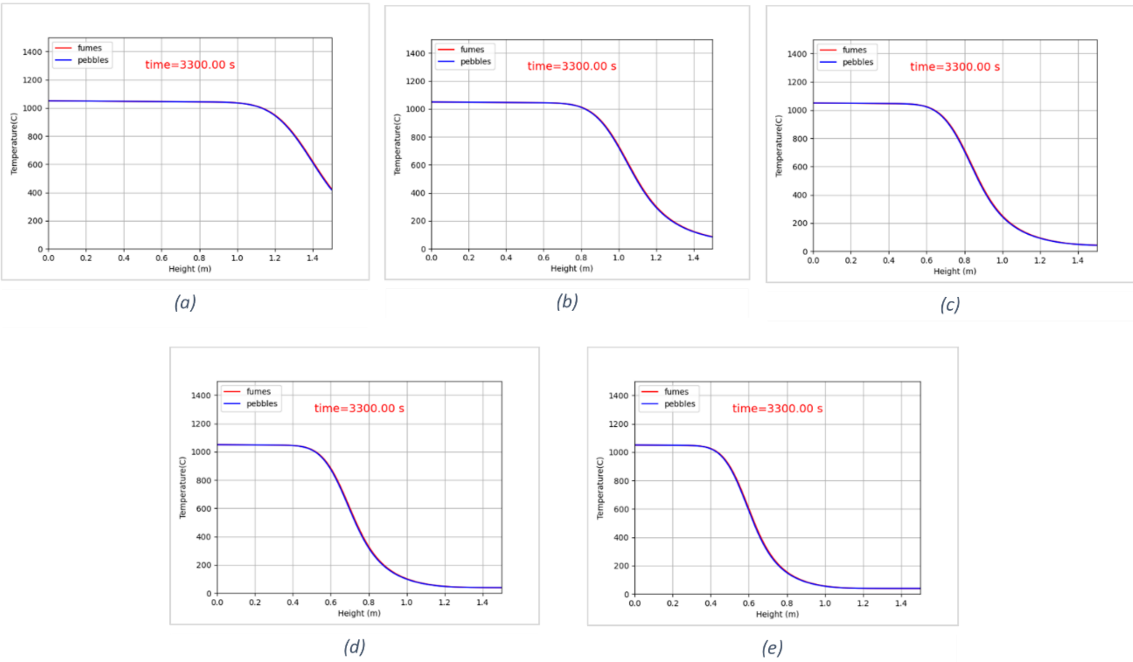

Figure 4.10: Sensitivity of C_{p_s} (a) -40% (b) -20% (c) Original (d) +20% (c) +40%

As shown in Figure 4.10, a change in the specific heat capacity of the solids affect how fast the PBTES would be charged. At lower C_{p_s}, the temperature of the PBTES rises quicker and vice versa. A crucial point could also be noted in Figure 4.10a – where the temperature of the HTF exiting after charging increased drastically, on the need to balance the specific heat capacity of the material with the charging time and/or PBTES height, to ensure that energy is not wasted by allowing high HTF temperatures at the PBTES exit in the charging phase, but to create a design that would guarantee the maximum extraction of energy from the high temperature charging fumes.

4.4.3. Solid Particle Diameter

Changing the solid diameter of the PBTES actually leads to more changes than expected in the PBTES. An increase in the diameter caused a reduction in the slope of the thermal front/thermal gradient of the temperature distribution in the PBTES and vice versa.

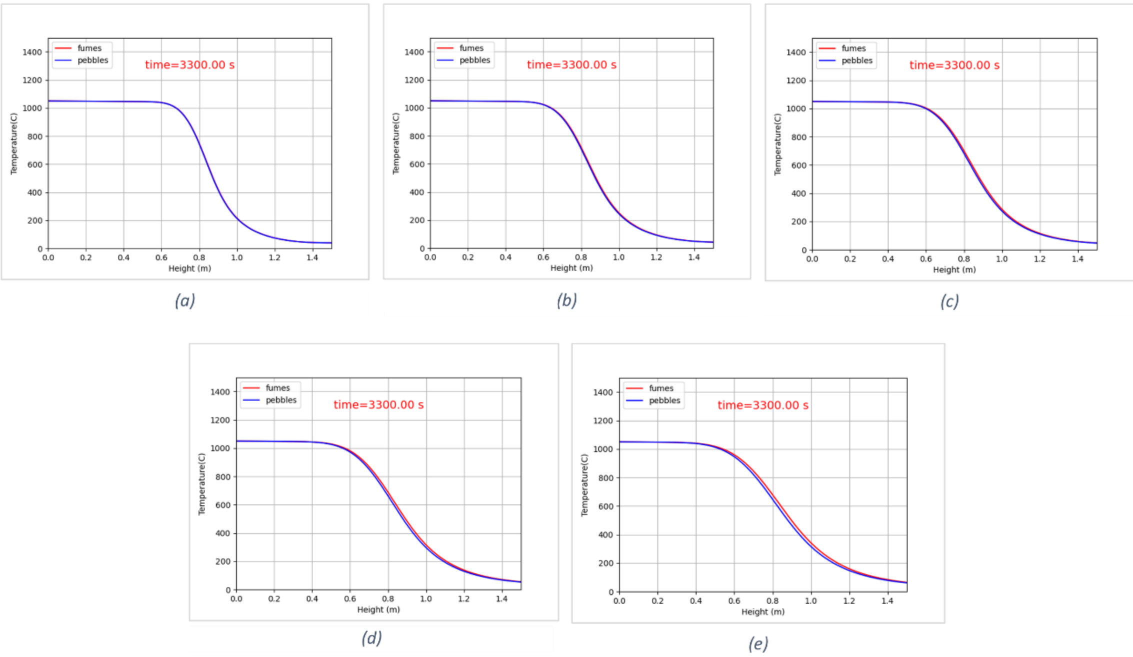

Figure 4.11: Sensitivity of D_p to T (a) – 50% (b) Original (c) +50% (d) +100% (e) +150%

This indicates that a change in the solid particle diameter significantly affects the effective thermal conductivity of the PBTES, and this change is largely attributed to the radiation contribution to the effective thermal conductivity which is directly proportional to the effective length for radiation between particles or particle diameter in this scenario. A noticeable trend of slope separation between the particle and fluid temperature distributions could also be observed from Figure 4.11, and this could be attributed to the growing prominence of the thermal gradients inside the solid as the solid particles increase in size. D_p also has an effect on the pressure drop obtainable in the PBTES as shown in Figure 4.12 below. Lower solid particle sizes lead to larger pressure drops and vice versa.

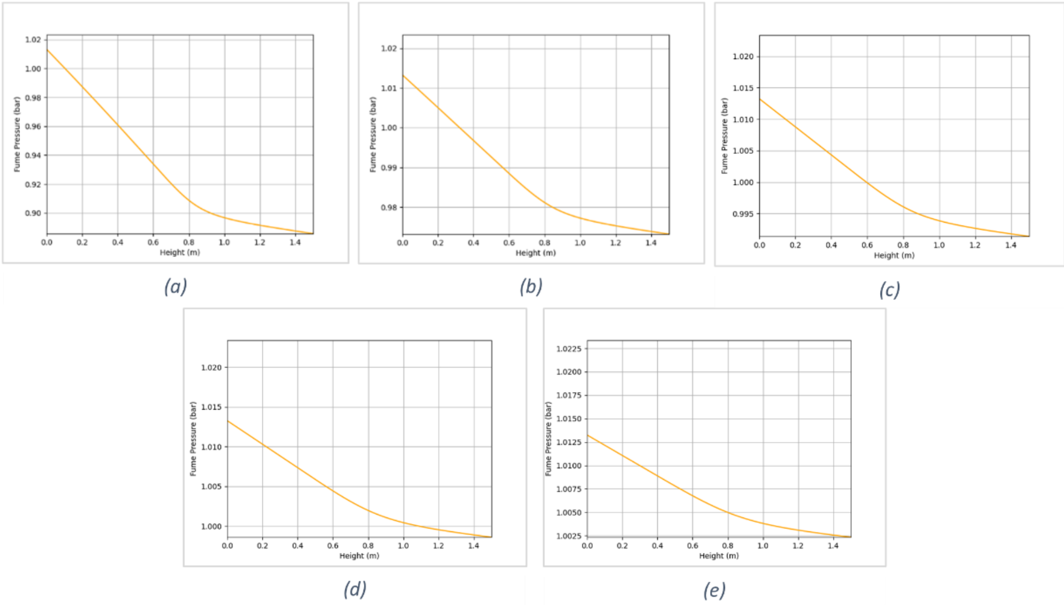

Figure 4.12: Sensitivity of D_p to P (a) – 50% (b) Original (c) +50% (d) +100% (e)+150%

4.5. Proposed Further Improvements

Every model has its limitations, and despite the fact that the model understudied was actually an improvement to a previous model, there are still further improvements that could be made within the scope of its pre-defined numerical robustness, and they are captured as follows:

i. **Modelling of PBTES Idling phase:** The model could be improved by adding another phase to its simulation scope called the idling phase. At the moment, the model only simulates charging and discharging phase, assuming that discharging occurs immediately after charging. However, this most likely would not always be the case in the real world and it would be interesting to have the idling phase model to simulate what happens to the PBTES when it is not in use for charging or discharging.

ii. **Improving the robustness of U_{loss}:** Despite the fact that the formulation for U_{loss} was demonstrated in detail, the complexity of its development for a general case made it difficult to build a robust function for it within the time constraints of this thesis, leading to the use of a constant input value. However, this could be improved by either following through with building the robust function or assigning U_{loss} to vary as a function of the PBTES temperature evolution, because this is actually the case in actual real-world scenarios.

iii. **Improving thermal conductivity discretization:** The resolution of the differential of the diffusive or conduction term used in the model (which is similar to what is obtainable in literature) treats the thermal conductivity's differential with respect to space as negligible, even though heavily dependent on temperature. This is a very practical approximation, especially considering the use of smaller spatial mesh sizes. However, with more steeper changes in temperature or the employment of different materials across the flow direction of the PBTES, this accuracy of this current model could likely wane. A solution to this is to deal with the conductive term differential as shown in the equation below, with the thermal conductivity values at each node being calculated using the harmonic mean of the thermal conductivity of its surrounding nodes, by employing a contrast with finite volume formulation methodology.

$$\frac{d}{dz}\left(\lambda\frac{dT}{dz}\right) = \lambda\frac{dT^2}{dz^2} + \frac{d\lambda}{dz}\frac{dT}{dz}$$

5. Conclusion

The urgency of the need to decarbonize and optimize the energy usage the steel industry is largely looming and ArcelorMittal as a leading global steel company is committed to developing solutions that contribute to meeting this need. Amongst the various strategies employed by the global conglomerate is the employment of regenerative heat exchangers to recover waste heat from the steel plant processes. Pebble bed heaters – a type of packed bed storage has shown to be a promising regenerative heat exchanger with the ability to cope with the complex nature and characteristics of the evolution of the waste heat given off in steel plants. Exploring these possibilities necessitated that numerical models be developed for the purpose of aiding and optimizing the design process of the PBTES to be incorporated into the steel processes, thus, the thesis was focused on the development of such models for the pebble heaters, with an aim to improve the robustness of an already existing model, while developing new models for proposed novel PBTES designs.

First, a literature review on modelling techniques and its paraphernalia was carried out, afterwards, a series of improvement proposals were established and implemented. The improved model was a 1D two-equation model, numerically computed using the finite difference method with an implicit time integration scheme. The model was verified and also validated using experimental data reported from literature sources. Afterwards, a sensitivity analysis was performed as a preview of a design optimisation study, and it revealed that the solid thermal conductivity did not heavily impact the temperature evolution of the PBTES due to the very low fluid thermal conductivity that often led to low overall effective thermal conductivity. The sensitivity study also showed that the specific heat capacity of the solid directly impacts the rate of charging and discharging of the PBTES as well as the exit temperature of the HTF, hinting that optimisation of the bed height, charging time and specific heat capacity needed to be made, to ensure maximal utilization of the energy of the waste heat flue gases. The pebble bed diameter was also shown to affect the thermal front of the PBTES, as higher solid particle diameters caused an increased radiation contribution to the effective thermal conductivity and vice versa. Lower solid particle size was also shown to increase the pressure drop across the PBTES bed and vice versa.

5.1. Further Work

Due to the fact that the thesis internship extends beyond the thesis termination timeline, some further work to be carried out, ensues viz:

i. Incorporation of radial PBTES configuration to the model
ii. Modelling of novel PBTES designs proposed by ArcelorMittal.
iii. Proper Parametric analysis for design optimisation using semi-industrial and industrial use cases.

References

[1] I. Energy Agency, “Iron and Steel Technology Roadmap Towards more sustainable steelmaking Part of the Energy Technology Perspectives series.” [Online]. Available: www.iea.org/t&c/

[2] ArcelorMittal, “Climate Action Report 2,” 2021.

[3] S. Trevisan, Y. Jemmal, R. Guedez, and B. Laumert, “Packed bed thermal energy storage: A novel design methodology including quasi-dynamic boundary conditions and techno-economic optimization,” *J Energy Storage*, vol. 36, Apr. 2021, doi: 10.1016/j.est.2021.102441.

[4] P. Klein, T. H. Roos, and T. J. Sheer, “Experimental investigation into a packed bed thermal storage solution for solar gas turbine systems,” in *Energy Procedia*, Elsevier Ltd, 2014, pp. 840–849. doi: 10.1016/j.egypro.2014.03.091.

[5] B. Kilkovský, “Review of design and modeling of regenerative heat exchangers,” *Energies*, vol. 13, no. 3. MDPI AG, 2020. doi: 10.3390/en13030759.

[6] I. Ortega-Fernández and J. Rodríguez-Aseguinolaza, “Thermal energy storage for waste heat recovery in the steelworks: The case study of the REslag project,” *Appl Energy*, vol. 237, pp. 708–719, Mar. 2019, doi: 10.1016/j.apenergy.2019.01.007.

[7] T. Esence, A. Bruch, S. Molina, B. Stutz, and J. F. Fourmigué, “A review on experience feedback and numerical modeling of packed-bed thermal energy storage systems,” *Solar Energy*, vol. 153. Elsevier Ltd, pp. 628–654, 2017. doi: 10.1016/j.solener.2017.03.032.

[8] S. Trevisan and R. Guedez, “Design optimization of an innovative layered radial-flow high-temperature packed bed thermal energy storage,” *J Energy Storage*, vol. 83, Apr. 2024, doi: 10.1016/j.est.2024.110767.

[9] T. E. W. Schumann, “HEAT TRANSFER: A LIQUID FLOWING THROUGH A POROUS PRISM,” 1929.

[10] K. A. R. Ismail and R. Stuginsky, “A parametric study on possible ®xed bed models for pcm and sensible heat storage,” 1999.

[11] W. H. Gerstle, N. R. Schroeder, L. P. McLaughlin, C. K. Ho, H. F. Laubscher, and S. Kao, “Experimental testing and computational modeling of a radial packed bed for thermal energy storage,” *Solar Energy*, vol. 264, Nov. 2023, doi:

10.1016/j.solener.2023.111993.

[12] R. Anderson, S. Shiri, H. Bindra, and J. F. Morris, “Experimental results and modeling of energy storage and recovery in a packed bed of alumina particles,” *Appl Energy*, vol. 119, pp. 521–529, Apr. 2014, doi: 10.1016/j.apenergy.2014.01.030.

[13] F. Marongiu, S. Soprani, and K. Engelbrecht, “Modeling of high temperature thermal energy storage in rock beds – Experimental comparison and parametric study,” *Appl Therm Eng*, vol. 163, Dec. 2019, doi: 10.1016/j.applthermaleng.2019.114355.

[14] R. Anderson, L. Bates, E. Johnson, and J. F. Morris, “Packed bed thermal energy storage: A simplified experimentally validated model,” *J Energy Storage*, vol. 4, pp. 14–23, Dec. 2015, doi: 10.1016/j.est.2015.08.007.

[15] L. Zou, D. O’Grady, G. Hu, and R. Hu, “Explicit Modeling of Pebble Temperature in the Porous-medium Framework for Pebble-bed Reactors Applications,” Mar. 2021. [Online]. Available: www.anl.gov.

[16] B. Xu, P. W. Li, and C. L. Chan, “Extending the validity of lumped capacitance method for large Biot number in thermal storage application,” *Solar Energy*, vol. 86, no. 6, pp. 1709–1724, Jun. 2012, doi: 10.1016/j.solener.2012.03.016.

[17] R. Pfeffer, “Heat and mass transport in multiparticle systems,” *Industrial and Engineering Chemistry Fundamentals*, vol. 3, no. 4, pp. 380–383, Nov. 1964, doi: 10.1021/I160012A018/ASSET/I160012A018.FP.PNG_V03.

[18] B. Alazmi and K. Vafai, “Analysis of Variants Within the Porous Media Transport Models,” 2000.

[19] J. P. Coutiert and E. A. Farber, “TWO APPLICATIONS OF A NUMERICAL APPROACH OF HEAT TRANSFER PROCESS WITHIN ROCK BEDS,” 1982.

[20] N. Wakao, S. Kaguei, and T. Funazkri, “EFFECT OF FLUID DISPERSION COEFFICIENTS ON PARTICLE-TO-FLUID HEAT TRANSFER COEFFICIENTS IN PACKED BEDS CORRELATION OF NUSSELT NUMBERS”.

[21] D. A. Nield, “Estimation of the stagnant thermal conductivity of saturated porous media,” *Int J Heat Mass Transf*, vol. 34, no. 6, pp. 1575–1576, Jun. 1991, doi: 10.1016/0017-9310(91)90300-4.

[22] P. Zehner and E. U. Schlünder, “Wärmeleitfähigkeit von Schüttungen bei mäßigen Temperaturen,” *Chemie Ingenieur Technik*, vol. 42, no. 14, pp. 933–941, Jul. 1970,

doi: 10.1002/CITE.330421408.

[23] S. Sumin Sih and J. W. Barlow, “The prediction of the emissivity and thermal conductivity of powder beds,” *Particulate Science and Technology*, vol. 22, no. 3, pp. 291–304, 2004, doi: 10.1080/02726350490501682a.

[24] G. Breitbach and H. Barthels, “RADIANT HEAT TRANSFER IN THE HIGH TEMPERATURE REACTOR CORE AFTER FAILURE OF THE AFTERHEAT REMOVAL SYSTEMS.,” *Nucl Technol*, vol. 49, no. 3, pp. 392–399, 1980, doi: 10.13182/NT80-A17687.

[25] P. CHENG and C.-T. HSU, “HEAT CONDUCTION,” *Transport Phenomena in Porous Media*, pp. 57–76, Jan. 1998, doi: 10.1016/B978-008042843-7/50003-9.

[26] S. Ergun and A. A. Orning, “Fluid Flow through Randomly Packed Columns and Fluidized Beds,” *Ind Eng Chem*, vol. 41, no. 6, pp. 1179–1184, Jun. 2002, doi: 10.1021/IE50474A011.

[27] M. Hänchen, S. Brückner, and A. Steinfeld, “High-temperature thermal storage using a packed bed of rocks - Heat transfer analysis and experimental validation,” *Appl Therm Eng*, vol. 31, no. 10, pp. 1798–1806, Jul. 2011, doi: 10.1016/j.applthermaleng.2010.10.034.

[28] A. Meier, C. Winkler, and D. Wuil, “Solar Energy Materials Experiment for modeling high temperature rock bed storage,” 1991.

[29] “Cantera.” Accessed: Jun. 16, 2024. [Online]. Available: https://cantera.org/

[30] CTTC and UPC, “FORMULAE FOR THE RESOLUTION OF FLUID DYNAMICS AND HEAT AND MASS TRANSFER PROBLEMS,” 2023.

[31] T. Esence, A. Bruch, S. Molina, B. Stutz, and J. F. Fourmigué, “A review on experience feedback and numerical modeling of packed-bed thermal energy storage systems,” *Solar Energy*, vol. 153. Elsevier Ltd, pp. 628–654, 2017. doi: 10.1016/j.solener.2017.03.032.

[32] S. Sumin Sih and J. W. Barlow, “The prediction of the emissivity and thermal conductivity of powder beds,” *Particulate Science and Technology*, vol. 22, no. 3, pp. 291–304, 2004, doi: 10.1080/02726350490501682a.

[33] J. Beek, “DESIGN OF PACKED CATALYTIC REACTORS. Adv Chem Eng,” 1962.

[34] J. Tušek, A. Kitanovski, I. Prebil, and A. Poredoš, “Dynamic operation of an active magnetic regenerator (AMR): Numerical optimization of a packed-bed AMR,” in

International Journal of Refrigeration, Sep. 2011, pp. 1507–1517. doi: 10.1016/j.ijrefrig.2011.04.007.

[35] Yano M, Douglass Penn J, Konidaris J, and T Patera A, “Math, Numerics & Programming (for Mechanical Engineers),” p. 403, 2012.

[36] E. Turkoz and M. Celik, “AETHER: A simulation platform for inductively coupled plasma,” *J Comput Phys*, vol. 286, pp. 87–102, Apr. 2015, doi: 10.1016/j.jcp.2015.01.027.

[37] “LAPACK: gesv: factor and solve, mixed precision.” Accessed: Jun. 20, 2024. [Online]. Available: https://netlib.org/lapack/explore-html/d8/dc6/group__gesv__mixed.html

[38] K. R. Muske, J. W. Howse, G. A. Hansen, and D. J. Cagliostro, “Los Alamos National Laboratory Advanced Control of Operations in the Blast Furnace Project Phase One Effort Documentation: Optimal Operation and Control of the Blast Furnace Stoves,” 1999.

[39] M. Hänchen, S. Brückner, and A. Steinfeld, “High-temperature thermal storage using a packed bed of rocks - Heat transfer analysis and experimental validation,” *Appl Therm Eng*, vol. 31, no. 10, pp. 1798–1806, Jul. 2011, doi: 10.1016/j.applthermaleng.2010.10.034.

[40] A. Meier, C. Winkler, and D. Wuil, “Experiment for modeling high temperature rock bed storage,” *Solar Energy Materials*, vol. 24, pp. 255–264, 1991.

Appendices

Appendix A

Discretization coefficients for counter current configuration

Calculating the discretization coefficients for counter current configuration required recompilation of the discretization coefficients for the fluid equation given the change in convective term and the boundary conditions for just the discharging phase.

For HTF (fluid):

Internal nodes $(\mathbf{0 < z < nz - 1})$

From equation 3.46

$$\frac{T_{f,z} - T_{f,z}{}^{o}}{\Delta t} = \frac{u_{f,z}}{\varepsilon \Delta z}\left(T_{f,z+1} - T_{f,z}\right) + \frac{\alpha_{f,z}\left(T_{f,z+1} - 2T_{f,z} + T_{f,z-1}\right)}{\Delta z^2} + \beta_{f,z}\left(T_{s,z} - T_{f,z}\right) + \gamma_{f,z}\left(T_{ambient} - T_{f,z}\right)$$

Re-arranging the equation gives

$$\left(-\frac{\alpha_{f,z}\Delta t}{\Delta z^2}\right)T_{f,z-1} + \left(1 + \frac{2\alpha_{f,z}\Delta t}{\Delta z^2} + \frac{u_f\Delta t}{\varepsilon\Delta z} + \beta_{f,z}\Delta t + \gamma_{f,z}\Delta t\right)T_{f,z} + \left(-\frac{\alpha_{f,z}\Delta t}{\Delta z^2} - \frac{u_f\Delta t}{\varepsilon\Delta z}\right)T_{f,z+1} + \left(-\beta_{f,z}\Delta t\right)T_{s,z} + \gamma_{f,z}\Delta t T_{ambient} = T_{f,z}{}^{o}$$

Introducing discretization coefficients gives:

$$\boldsymbol{a_{N_{f,z}}T_{f,z-1} + a_{P_{f,z}}T_{f,z} + a_{S_{f,z}}T_{f,z+1} + b_{P_{f,z}}T_{s,z} = T_{f,z}{}^{o} + D}$$

Where:

$$a_{N_{f,z}} = -\frac{\alpha_{f,z}\Delta t}{\Delta z^2}$$

$$a_{S_{f,z}} = -\frac{\alpha_{f,z}\Delta t}{\Delta z^2} - \frac{u_f\Delta t}{\varepsilon\Delta z}$$

$$a_{P_{f,z}} = 1 + \frac{2\alpha_{f,z}\Delta t}{\Delta z^2} + \frac{u_f\Delta t}{\varepsilon\Delta z} + \beta_{f,z}\Delta t + \gamma_{f,z}\Delta t$$

$$b_{P_{f,z}} = -\beta_{f,z}\Delta t$$

$$D = \gamma_{f,z}\Delta t T_{ambient}$$

Boundary node **($\mathbf{z = 0}$)**

Since the fluid comes in from the bottom of the PBTES during the discharging phase in the counter current configuration, the boundary at $z = 0$ corresponds to the exit of the HTF. Thus, from equation 3.46,

$$\frac{T_{f,0} - T_{f,0}{}^{o}}{\Delta t} = \frac{u_{f,0}}{\varepsilon \Delta z}\left(T_{f,1} - T_{f,0}\right) + \frac{\alpha_{f,0}\left(T_{f,1} - T_{f,0}\right)}{\Delta z^2} + \beta_{f,0}\left(T_{s,0} - T_{f,0}\right) + \gamma_{f,0}\left(T_{ambient} - T_{f,0}\right)$$

Re-arranging the equation gives:

$$\left(1 + \frac{u_{f,0}\Delta t}{\varepsilon \Delta z} + \frac{\alpha_{f,0}\Delta t}{\Delta z^2} + \beta_{f,0}\Delta t + \gamma_{f,0}\Delta t\right)T_{f,0} + \left(-\frac{u_{f,0}\Delta t}{\varepsilon \Delta z} - \frac{\alpha_{f,0}\Delta t}{\Delta z^2}\right)T_{f,1} + \left(-\beta_{f,0}\Delta t\right)T_{s,0} = T_{f,0}{}^{o} + \gamma_{f,0}\Delta t T_{ambient}$$

Introducing discretization coefficients gives:

$$\boldsymbol{a_{P_f,0}T_{f,0} + a_{S_f,0}T_{f,1} + b_{P_f,0}T_{s,0} = T_{f,0}{}^{o} + D}$$

Where:

$$a_{S_f,0} = -\frac{u_{f,0}\Delta t}{\varepsilon \Delta z} - \frac{\alpha_{f,0}\Delta t}{\Delta z^2}$$

$$a_{P_f,0} = 1 + \frac{u_{f,0}\Delta t}{\varepsilon \Delta z} + \frac{\alpha_{f,0}\Delta t}{\Delta z^2} + \beta_{f,0}\Delta t + \gamma_{f,0}\Delta t$$

$$b_{P_f,0} = -\beta_{f,0}\Delta t$$

$$D = \gamma_{f,0}\Delta t T_{ambient}$$

Boundary node **($\mathbf{z = nz - 1}$)**

Since the fluid comes in from the bottom of the PBTES during the discharging phase in the counter current configuration, the boundary at $z = nz - 1$ corresponds to the inlet of the HTF. Thus, from equation 3.46,

$$\frac{T_{f,nz-1} - T_{f,nz-1}{}^{o}}{\Delta t} = \frac{u_{f,nz-1}}{\varepsilon \Delta z}\left(T_{HTF,in} - T_{f,nz-1}\right) + \frac{\alpha_{f,nz-1}\left(T_{f,nz-2} - 2T_{f,nz-1} + T_{HTF,\ in}\right)}{\Delta z^2} + \beta_{f,nz-1}\left(T_{s,nz-1} - T_{f,nz-1}\right) + \gamma_{f,nz-1}\left(T_{ambient} - T_{f,nz-1}\right)$$

Re-arranging the equation gives:

$$\left(-\frac{\alpha_{f,nz-1}\Delta t}{\Delta z^2}\right) T_{f,nz-2} + (1 + \frac{2\alpha_{f,nz-1}\Delta t}{\Delta z^2} + \frac{u_{f,nz-1}\Delta t}{\varepsilon \Delta z} + \beta_{f,nz-1}\Delta t + \gamma_{f,nz-1}\Delta t)\, T_{f,nz-1} + (-\beta_{f,nz-1}\Delta t) T_{s,nz-1} = T_{f,nz-1}{}^{o} + \left(\frac{\alpha_{f,nz-1}\Delta t}{\Delta z^2} + \frac{u_{f,nz-1}\Delta t}{\varepsilon \Delta z}\right) T_{HTF,in} + \gamma_{f,nz-1}\Delta t T_{ambient}$$

Introducing discretization coefficients gives:

$$\boldsymbol{a_{N_f,nz-1} T_{f,nz-2} + a_{P_f,nz-1} T_{f,nz-1} + b_{P_f,nz-1} T_{s,nz-1} = T_{f,nz-1}{}^{o} + C + D}$$

Where:

$$a_{N_f,nz-1} = -\frac{\alpha_{f,nz-1}\Delta t}{\Delta z^2}$$

$$a_{P_f,nz-1} = 1 + \frac{2\alpha_{f,nz-1}\Delta t}{\Delta z^2} + \frac{u_{f,nz-1}\Delta t}{\varepsilon \Delta z} + \beta_{f,nz-1}\Delta t + \gamma_{f,nz-1}\Delta t$$

$$b_{P_f,0} = -\beta_{f,nz-1}\Delta t$$

$$C = \left(\frac{\alpha_{f,nz-1}\Delta t}{\Delta z^2} + \frac{u_{f,nz-1}\Delta t}{\varepsilon \Delta z}\right) T_{HTF,in}$$

$$D = \gamma_{f,nz-1}\Delta t T_{ambient}$$

The newly derived discretization equations and co-efficients were put into matrix equations and solved as previously described in the main body of the report, to obtain the results for the discharging phase during the counter current configuration.

Appendix B

Dimensionless Numbers

The formulation of the dimensionless numbers mentioned in the main text could be seen below:

Reynolds Number (Re)

$$\mathrm{Re} = \frac{\rho u D}{\mu}$$

Prandtl Number (Pr)

$$Pr = \frac{\mu c_P}{\lambda}$$

Grashof's Number (Gr)

$$Gr = \frac{g\beta\rho^2\Delta\theta X^3}{\mu^2}$$

g = gravitational acceleration

$X =$ Characteristic length (m)

β = Volumetric thermal expansion coefficient = $\frac{1}{\rho}\left(\frac{\partial P}{\partial T}\right)_P$

For gases, $\beta = \frac{1}{T}$

Raleigh's number (Ra)

$$Ra = GrPr$$

Nusselt Number (Nu)

$$\mathrm{Nu} = \frac{hX}{\lambda} = f(\mathrm{Re},\mathrm{Pr})/f(Gr,\mathrm{Pr})\ \ for\ Forced/Natural\ \ Convection$$

Biot's number (Bi)

$$Bi = \frac{hX}{\lambda}$$